LJMU Research Online

Omondi, RO, Bellam, R, Ojwach, SO, Jaganyi, D and Fatokun, AA

 Palladium(II) complexes of tridentate bis(benzazole) ligands: Structural, substitution kinetics, DNA interactions and cytotoxicity studies.

http://researchonline.ljmu.ac.uk/id/eprint/13474/

Article

For more information please contact researchonline@ljmu.ac.uk

Palladium(II) complexes of tridentate bis(benzazole) ligands: structural, substitution kinetics, DNA interactions and cytotoxicity studies

Reinner O. Omondi[a], Rajesh Bellam[a], Stephen O. Ojwach[a*], Deogratius Jaganyi[b, c], Amos A. Fatokun[d*]

[a] School of Chemistry and Physics, University of KwaZulu-Natal, Private Bag X01, Scottsville, Pietermaritzburg 3209, South Africa.

[b] School of Science, College of Science and Technology, University of Rwanda, P.O. Box 4285, Kigali, Rwanda.

[c] Department of Chemistry, Faculty of Applied Sciences, Durban University of Technology, P.O. Box 1334, Durban 4000, South Africa

[d] Centre for Natural Products Discovery (CNPD), School of Pharmacy and Biomolecular Sciences, Faculty of Science, Liverpool John Moores University, Liverpool L3 3AF, UK.

Abstract

Reactions of 2,6-bis(benzimidazol-2-yl)pyridine (**L₁**), 2,6-bis(benzoxazol-2-yl)pyridine (**L₂**), and 2,6-bis(benzothiazol-2-yl)pyridine (**L₃**) with [Pd(NCMe)$_2$Cl$_2$] in the presence of NaBF$_4$ afforded the corresponding Pd(II) complexes, [Pd(**L₁**)Cl]BF$_4$, **PdL₁**; [Pd(**L₂**)Cl]BF$_4$, **PdL₂**; [Pd(**L₃**)Cl]BF$_4$, **PdL₃**; respectively, while reaction of bis[(1H-benzimidazol-2-yl)methyl]amine (**L₄**)   with [Pd(NCMe)$_2$Cl$_2$] afforded complex [Pd(**L₄**)Cl]Cl, **PdL₄**. Characterisation of the complexes was accomplished using NMR, IR, MS, elemental analyses and single crystal X-ray crystallography. Ligand substitution kinetics of these complexes by biological nucleophiles thiourea (**Tu**), L-methionine (**L-Met**) and guanosine 5′-diphosphate disodium salt (**5-GMP**) were examined under *pseudo*-first order conditions. The reactivity of the complexes decreased in the order: **PdL₁** > **PdL₂** > **PdL₃** > **PdL₄**, ascribed to electronic effects. Density functional theory (DFT) supported this trend. Studies of interaction of the Pd(II) complexes with calf thymus DNA (CT-DNA) revealed strong binding affinities *via* intercalative binding mode. Molecular docking studies established associative non-covalent interactions between the Pd complexes and DNA. The *in vitro* cytotoxic activities of **PdL₁**-**PdL₄** were assessed in cancer cell lines HeLa and MRC5-SV2 and a normal cell line MRC-5, using the 3-(4,5-Dimethyl-2-thiazolyl)-2,5-diphenyl-2H-tetrazolium bromide (MTT) assay. **PdL₁** exhibited cytotoxic potency and selectivity against HeLa cell that was comparable to cisplatin's. Complex **PdL₁**, unlike cisplatin, did not significantly induce caspase-dependent apoptosis.

Key words

*Corresponding authors: ojwach@ukzn.ac.za (SO Ojwach); A.A.Fatokun@ljmu.ac.uk (AA Fatokun)

1 Introduction

Despite the success of cisplatin in chemotherapy, its application is limited due to severe side effects, development of drug resistance and limited solubility [1-4]. The interaction of platinum complexes with sulfur containing biomolecules, such as glutathione, L-methionine and L-cysteine has been associated with negative effects such as gastrointestinal toxicity, nephrotoxicity, neurotoxicity, cardiotoxicity, and ototoxicity. These drawbacks have triggered the search for new metallo-drugs with improved specificity and efficacy in tumour treatment. With the rise of an exciting number of antineoplastic properties of other transition metals, the attention is gradually shifting beyond the use of platinum [5-17]. It is well documented that among the non-platinum based compounds, Pd(II) complexes seem to be the most promising class due to their structural similarity to Pt(II) complexes [18-25]. In addition, Pd(II) compounds display higher cytotoxicity, selectivity and better solubility than those of the conventional platinum drugs.

However, the rates of ligand-exchange kinetics of Pd(II) complexes are *ca*. 10^3-10^5 times faster than the corresponding Pt(II) compounds [26]. These high reactivities do not allow Pd(II) complexes to maintain their structural identity in the cytoplasm long enough to reach the target, DNA, and has slowed down their use as anti-cancer agents   To overcome this drawback, a judicious choice of the inert chelating ligands is crucial to reduce the kinetic lability of the Pd(II) complexes, and hence maximise their cytotoxic activity [7, 27-29].

Reports by Bugarčić [30] confirm that steric crowding improves interaction with the DNA and antitumour activity of metal complexes. The phenomenon, is explained by the slower kinetic reactivity of the complexes that enables them to reach the DNA, without much interference from other biological molecules in the cytoplasm. Contrarily, steric hindrance of the spectator ligands can also have a negative influence on the substitution kinetics, DNA-/protein-binding ability and cytotoxic activity [31, 32]. In a previous study, we examined the role of heteroatoms on the substitution kinetics and cytotoxicity of Ru(III) complexes anchored on (pyridyl)benzazole ligands [33]. The *in vitro* study demonstrated that the

2

complexes exhibited minimal cytotoxicity, which was attributed to their slow rate of substitution reactions. In this current work, our intention was to improve the cytotoxicity by regulating the rate of kinetic substitution using Pd(II) as a metal centre. Our hypothesis is that a combination of the slower spectator ligands and a more labile Pd metal would fine-tune the reactivity of the resultant complexes and give desirable cytotoxicity properties. In this contribution, we thus report the synthesis, structural characterisation of Pd(II) complexes of tridentate N^N^N 2,6-bis(benzazole) ligands and their substitutions reactions with biological donor nucleophiles; thiourea, **Tu**, L-methionine, **L-Met** (and guanosine-5'-monophosphate, **5'-GMP**. The choice of the nucleophiles was based on their high aqueous solubility, varied nucleophilicity and binding properties and steric influences. For example, **Tu** and **L-Met** were chosen as model nucleophiles for sulfur-containing biomolecules, which are abundant in the plasma (particularly proteins); while 5'-GMP was used as a model for binding to the nucleobases that are the main targets for metal-based antitumour drugs. The interaction of the complexes with calf-thymus DNA (CT-DNA) and intercalative agent ethidium bromide (EB) were investigated. Cytotoxic activities of the complexes on the cancer cell lines, human cervix adenocarcinoma (HeLa), human (foetal) lung carcinoma (MRC5-SV2) and normal human foetal lung fibroblast) cell line, (MRC-5), were also studied and are herein reported.

2. Experimental section

2.1 General considerations

All synthetic manipulations were performed under dry and oxygen free nitrogen atmosphere using standard Schlenk line techniques, unless otherwise stated. 32% hydrochloric acid (HCl), 25% ammonia solution, polyphosphoric acid, methanol and sodium carbonate were obtained from Merck. The chemicals, pyridine-2,6-dicarboxylic acid (99.0%), *o*-phenylenediamine (99.5%), 2-aminophenol (99.0%), 2-aminothiophenol (99.0%), iminodiacetic acid (≥98.0%), silver tetrafluoroborate (98.0%), thiourea (≥99.0%), L-methionine (≥98.0%), guanosine 5′-diphosphate disodium salt (≥96.0%), Hepes buffer (N-2-hydroxyethylpiperazine-N′-2-ethanesulfonic acid) (≥99.5%), ethidium bromide (EB) (95.0%), and calf thymus DNA (CT-DNA) were purchased from Merck and were used without further purification. Ligands

L_1, L_2 and L_3 were synthesised according to published procedure [34]. On the other hand, L_4 was prepared following the synthetic procedure described by Kopel et al.[35] The starting material, $PdCl_2(NCMe)_2$ was synthesised based on the reported procedure [36].

Cell culture reagents including Dulbecco's Modified Eagle Medium (DMEM), phosphate-buffered saline (PBS), trypsin (TrypLE), L-glutamine and antibiotic-antimycotic (anti-anti) solution were obtained from Life Technologies (ThermoFisher Scientific). Foetal Bovine Serum (FBS) was obtained from Sigma. Z-VAD-fmk was obtained from Tocris Bioscience (Bio-Techne) while DMSO (tissue culture grade), 3,4-Dihydro-5-[4-(1-piperidinyl)butoxyl]-1(2H)-isoquinolinone (DPQ), and 3-(4,5-Dimethyl-2-thiazolyl)-2,5-diphenyl-2H-tetrazolium bromide (MTT) were purchased from Sigma-Aldrich (UK). Cell lines were obtained originally from the European Collection of Authenticated Cell Cultures (ECACC).

Nuclear magnetic resonance spectra were acquired at 400 MHz for ^{1}H, 100 MHz for ^{13}C on a Bruker Avance spectrometer in DMSO-d6 solution at room temperature. Chemical shifts were determined relative to internal tetramethylsilane and are given in δ (ppm) and all coupling constants (J) are reported in hertz, (Hz). Elemental analyses were carried out using CHNS-O Flash 2000 thermo scientific analyser. Mass spectral analyses were measured on an LC Premier micro-mass spectrometer. The infrared spectra were recorded on Agilent Technologies Cary 630 in the 3800- 600 cm^{-1} range. X-ray data were recorded on a Bruker Apex Duo diffractometer equipped with an Oxford Instrument. Substitution kinetic reactions were performed on an Applier Photophysics SX 20 stopped-flow reaction analyser coupled with an online data acquisition system with controlled temperature within ± 0.1 °C. The wavelengths for the kinetic analysis were predetermined on Varian Cary 100 Bio UV-visible spectrophotometer with an attached Varian Peltier temperature-controller within ± 0.1°C and an online kinetic application system. The pH measurements were recorded on a Jenway 4330 conductivity/pH meter equipped with a Jenway glass microelectrode calibrated with standard buffer solutions of pH 4.0, 7.0 and 10.0.

2.3 Syntheses of palladium metal complexes

*2.3.1 [{2,6-bis(benzimidazol-2-yl)pyridine}PdCl]BF₄ (**PdL₁**)*

To a solution of $PdCl_2(NCMe)_2$ (0.10 g, 0.39 mmol) in CH_2Cl_2 (30 mL) was added **L₁** (0.12 g, 0.39 mmol) and $NaBF_4$ (0.04, 0.39 mmol) to give a yellow solution. The resultant mixture was stirred for 12 h and filtred through a short pad of Celite to remove the precipitate of NaCl. Hexane (10 mL) was added to the filtrate to afford **PdL₁** as a yellow solid. Yield: 0.12 g (57%). ^1H NMR (400 MHz, DMSO-d₆): δ_H (ppm): 7.24-7.33 (m, 4H); 7.57 (d, $^3J_{HH}$ = 8.1, 2H); 7.93 (d, $^3J_{HH}$ = 8.1, 2H); 8.06 (d, $^3J_{HH}$ = 8.0, 2H); 8.35 (t, 1H, $^3J_{HH}$ = 7.9, H). ^{13}C NMR (DMSO-d₆): δ_C (ppm): 114.62; 116.73; 122.05; 124.91; 140.06; 142.87; 147.54; 152.97. FT-IR (cm⁻¹): υ(N-H) = 2728; υ(C=C) =1571; υ(C=N) = 1476. TOF MS ES⁺, m/z (%) = 451 [M,100]⁺. HRMS-ESI [M + 3H]⁺: m/z calc: 449.9738; found: 449.9730. Anal. Calcd (%) for $C_{19}H_{13}BClF_4N_5Pd$: C, 42.26; H, 2.43; N, 12.97. Found (%): C, 41.95; H, 2.70; N, 12.71

Complexes **PdL₂-PdL₃** were prepared following the protocol described for **PdL₁** using appropriate ligands.

2.3.2 [{2,6-bis(benzoxazol-2-yl)pyridine}PdCl]BF₄ (**PdL₂**)

Ligand **L₂** (0.12 g, 0.39 mmol), $PdCl_2(NCMe)_2$ (0.10 g, 0.39 mmol) and $NaBF_4$ (0.04 g, 0.39 mmol). Off yellow solid. Single crystals were grown by allowing diethyl ether to diffuse into acetonitrile solution.Yield: 0.11 g (52%).^1H NMR (400 MHz, DMSO-d₆): δ_H (ppm): 7.53-7.55 (m, 2H, H$_a$,); 7.57-7.58 (m, 2H); 7.96 (t, $^3J_{HH}$ = 7.8, 4H); 8.34 (t, $^3J_{HH}$ = 8.0, 1H); 8.57 (d, $^3J_{HH}$ = 7.8, 2H). ^{13}C NMR (DMSO-d₆): δ_C (ppm): 111.54; 120.50; 125.31; 125.63; 126.61; 139.40; 141.14; 145.80; 150.61; 160.62. FT-IR (cm⁻¹): υ(C=C) =1544; υ(C=N) = 1408; υ(C-O) = 1036. LC MS/ESI⁺, m/z (%) = 453 [M, 100] ⁺. HRMS-ESI [M + H]⁺: m/z calc: 453.9581; found: 453.9575. Anal. Calcd (%) for $C_{19}H_{11}BClF_4N_3O_2Pd.CH_2Cl_2$: C, 42.10; H, 2.05; N, 7.75. Found (%): C, 41.72; H, 2.19; N, 7.36.

2.3.3 [{2,6-bis(benzothiazol-2-yl)pyridine}PdCl]BF₄ (**PdL₃**)

Ligand **L₃** (0.13 g, 0.39 mmol), $PdCl_2(NCMe)_2$ (0.10 g, 0.39 mmol) and $NaBF_4$ (0.04 g, 0.39 mmol). Off yellow solid. Yield: 0.14 g (63%). ^1H NMR (400 MHz, DMSO-d₆): δ_H (ppm): 7.57 (t, $^3J_{HH}$ = 7.2, 2H); 7.62 (t, $^3J_{HH}$ = 7.9, 2H); 8.17 (d, $^3J_{HH}$ = 8.1, 2H); 8.27 (dd, $^3J_{HH}$ = 8.1, 3H,); 8.49 (d, $^3J_{HH}$ = 7.2, 2H). ^{13}C NMR (DMSO-d₆): δ_C (ppm): 122.25; 122.74; 123.51; 126.28; 126.83; 135.52; 139.79; 150.54;

153.76; 167.69. FT-IR (cm^{-1}): υ(C=C) =1584; υ(C=N) = 1448; υ(C-S) = 1015. LC MS/ESI$^+$, *m/z (%)* = 485 [M, 100]$^+$. HRMS-ESI [M + H]$^+$: *m/z* calc: 485.9118; found: 485.9120. Anal. Calcd (%) for C$_{19}$H$_{11}$BClF$_4$N$_3$PdS$_2$: C, 39.75; H, 1.93; N, 7.32, S, 11.17. Found (%): C, 39.44; H, 1.68; N, 6.94, S, 10.94.

2.3.4 [{bis⟨(1H-benzimidazol-2-yl)methyl⟩ amine}PdCl]Cl (**PdL₄**)

To a solution of compound **L₄** (0.11 g, 0.39 mmol) in CH$_2$Cl$_2$ (15 mL) was added a solution of and PdCl$_2$(NCMe)$_2$ (0.10 g, 0.39 mmol) in CH$_2$Cl$_2$ (15 mL). The resultant yellow solution was stirred for 24 h and the product precipitated by the addition of hexane (10 mL) to give a white-yellowish solid. Single crystals were grown via vapour diffusion of diethyl ether into a saturated solution of **PdL₄** in DMSO. Yield: 0.10 g (51 %). ^{1}H NMR (400 MHz, DMSO-d$_6$): δ_H (ppm): 4.49 (dd, $^3J_{HH}$ = 7.4, 2H); 4.93 (dd, 2H, $^3J_{HH}$ = 7.4, 2H); 7.35-7.41 (m, 4H); 7.64-7.68 (m, 2H); 8.14 (s, 1H, NH); 8.27-8.31 (m, 2H); 13.90 (s, 2H, NH).^{13}C NMR (DMSO-d$_6$): δC (ppm): 51.39; 112.85; 116.90; 123.54; 124.09; 132.12; 138.91; 158.94. FT-IR (cm^{-1}): υ(N-H) = 3619; υ(C=C) =1589; υ(C=N) = 1433. LC MS/ESI$^+$, *m/z (%)* = 417 [M, 100]$^+$; 838 [2M, 10%]$^+$. HRMS-ESI [M + H]$^+$: *m/z* calc: 418.0051; found: 418.0060. Anal. Calcd (%) for C$_{16}$H$_{15}$Cl$_2$N$_5$Pd: C, 42.27; H, 3.33; N, 15.40. Found (%): C, 41.97; H, 3.52; N, 15.09.

2.4. Single crystal X-ray crystallography

X-ray data for complexes **PdL₂** and **PdL₄** were recorded on a Bruker Apex Duo diffractometer equipped with an Oxford Instruments Cryojet operating at 100(2) K and an Incoatec microsource operating at 30 W power. The data were collected with Mo Kα (λ = 0.71073 Å) radiation at a crystal-to-detector distance of 50 mm. The following conditions were used for the data collection: omega and phi scans with exposures taken at 30 W X-ray power and 0.50º frame widths using APEX2 [37]. The data were reduced with the programme SAINT[38] using outlier rejection, scan speed scaling, as well as standard Lorentz and polarisation correction factors. A SADABS semi-empirical multi-scan absorption correction was applied to the data. Direct methods, SHELXS-2014 andWinGX [39], were used to solve all three structures. All non-hydrogen atoms were located in the difference density map and refined anisotropically with SHELXL-2014. All hydrogen atoms were included as idealised contributors in the least squares

process. Their positions were calculated using a standard riding model with C-H$_{aromatic}$ distances of 0.93 Å and Uiso= 1.2 Ueq, C–H$_{methylene}$ distances of 0.99 Å and Uiso = 1.2 Ueq and C–H$_{methyl}$ distances of 0.98 Å and Uiso= 1.5 Ueq.

2.5 Kinetic and mechanistic measurements

All kinetic measurements were studied at physiological conditions (pH 7.2) in the presence of 25 mM Hepes buffer. In order to suppress the spontaneous hydrolysis of the complexes, 10 mM NaCl was added to the complex solution. The stock solution of the nucleophiles approximately 50-fold excess of the complex concentration was serially diluted with the aqueous solution to afford 40, 30, 20 and 10-fold in excess of the concentration of the complex to maintain pseudo-first-order conditions. The wavelengths chosen for the kinetic investigations were pre-determined by following the change in absorbance of the mixture of the metal complex and the nucleophile as a function of time using the UV-visible spectra. All reactions were initiated by mixing equal volumes of nucleophile and complex solutions directly in the stopped-flow instrument. Concentration dependence studies were investigated at a constant temperature of 298 K, while the temperature dependence reactions were studied from 298 to 328 K at an interval of 10 K. All kinetic reactions i.e. concentration and temperature dependent were initiated by mixing equal volumes of ligand and complex solutions directly in the stopped-flow instrument. The pseudo-first-order rate constants (k_{obs}), were obtained as the average of no less than 5-9 independent runs.

2.6 Density Functional Theoretical calculations and molecular docking

Computational calculations were performed using density functional theory (DFT) method executed by Gaussian 09W suite of programmes [40]. The structures were optimised using the hybrid Becke, 3-parameter, Lee-Yang-Parr at the standard Los Alamos National Laboratory 2 double ζ (LANL2DZ) basis set [41]. To incorporate solvent effects, the systems were fully optimised in aqueous solution using conductor like polarisable continuum implicit solvent model (CPCM) [42]. The calculations were done at a singlet spin ground state and at an overall charge of +1. Gauss View 5.0 programme was used to visualise the optimised minimum energy structures of the complexes under

investigation. Electronic chemical potential (μ), chemical hardness (η), chemical softness (σ) and global electrophilicity indices (ω) for the complexes were calculated as per literature methods [43]. Natural bonding orbitals (NBO) analysis was used to determine localised atomic charges in the complexes [40]. The complexes were **PdL₁-PdL₄** were docked onto the right-handed helix of normal double-stranded DNA (B-DNA) using HEX8.0 software [44]. The coordinates of all the complexes were optimised by Gaussian 09 programme and converted to Protein Data bank (PDB) using Mercury 3.3 software. The crystal structure of the B–DNA dodecamer d(CGCGAATTCGCG)$_2$ (PDB ID: 1BNA) was retrieved from the protein data bank [45]. The docked pose of 1BNA and each complex were viewed using UCSF CHIMERA software [46]. The docking protocol was repeated three times and almost similar docking poses were viewed in each of the runs. The E$_{(lowest\ energy\ pose)}$ value of each Pd complex and DNA interactional pose was examined.

2.7 DNA-binding experiments

2.7.1 Absorption spectral studies

The calf thymus-DNA (CT-DNA) binding experiments were performed at room temperature in 5 mM tris(hydroxymethyl)amino methane, Tris-HCl/50 mM NaCl buffer (pH = 7.2), stored at 4 °C in the dark and used within 4 days. A stock solution of the complex (5 mM) was prepared in 50 % DMSO. The concentration of CT-DNA was determined from a Beer-Lambert plot by measuring the absorption intensity at 260 nm, where the molar absorptivity of CT-DNA is about 6600 M^{-1} cm^{-1}. The absorbance ratio at 260 and 280 nm (A$_{260}$/A$_{280}$) was measured and found to be in the range of 1.8 to 1.9, indicating that the DNA was sufficiently free of protein. A fixed 20 μM concentration of each chloro Pd(II) complex, **PdL₁-PdL₄** was titrated spectrophotometrically with increasing CT-DNA concentrations (0 - 40 μM). The absorption spectra were obtained by adding the requisite amount of CT-DNA to both reference and sample solutions to eliminate the absorbance of CT-DNA. The Pd(II) complex-DNA solutions were allowed to incubate for 10 min in cuvette before the absorption spectra were recorded. The absorption changes were monitored at the metal-to-ligand charge transfer (MLCT) bands of the complexes as a function of

increasing concentration of CT-DNA. The binding affinities of Pd(II) complexes were calculated using the Wolfe-Shimer equation (1).

$$[DNA]/(\varepsilon_a-\varepsilon_f) = [DNA]/(\varepsilon_b-\varepsilon_f)+1/(K_b(\varepsilon_b-\varepsilon_f)) \tag{1}$$

where [DNA] is the concentration of CT-DNA, ε_a, ε_f and ε_b are the molar absorptivities of the titrated mixture (A_{obs}/[complex]), unbound Pd(II) complex and the Pd(II)/CT-DNA complex, respectively. K_b is calculated from the ratio of the slope to intercept in the plot of $[DNA]/(\varepsilon_a - \varepsilon_f)$ versus [DNA].

2.7.2 Fluorescence quenching studies

The fluorescence quenching experiments were performed using 3,8-diamino-5-ethyl-6-phenylphenanthridinium bromide (EB) to probe the competitive binding abilities of Pd(II) complexes on the CT-DNA. Fixed concentration of CT-DNA-EB (10 µM each of CT-DNA and EB) was prepared in 5 mM Tris-HCl/50 mM NaCl buffer (pH = 7.2). This solution was stored for 4 h at 4 °C. The competitive binding effects of the complexes, **PdL₁-PdL₄** on the DNA-EB complex were monitored by adding aliquot amounts of stock Pd(II) (5 mM) complexes solutions in incremental amounts to the CT-DNA+EB solutions. The decrease in the fluorescence emission was recorded within the wavelength range of 520 to 700 nm after excitation of the solutions at 500 nm. Before recording the spectra, the solutions were thoroughly mixed and incubated for 10 min at room temperature. The quenching efficiency of the complexes was analysed using the Stern-Volmer equation (2) [35].

$$I_o/I = 1 + K_{sv}[Q] = 1 + k_q\tau_0[Q] \tag{2}$$

where I_o and I are the emission intensities of CT-DNA+EB complex in the absence and following each addition of complex, respectively, and [Q] is the concentration of quencher (chloro Pd(II) complex). The Stern-Volmer (quenching) constant, K_{sv}, was determined from the slope of the linear plot of I_o/I versus [Q]. To have an insight into the kinetics of the competitive binding process, values of the bimolecular quenching rate constant, k_q were also computed using the Stern-Volmer equation, where τ_0 is the average fluorescence lifetime of the CT-DNA+EB complex in the absence of the quencher and its value is 23

nanoseconds at room temperature. The apparent binding constant, K_{app} was computed from the equation (3).

$$K_{EtBr}[\text{EtBr}] = K_{app}[\text{Q}] \tag{3}$$

where [Q] is the concentration of quencher causing 50% reduction in fluorescence intensity of CT-DNA+EtBr complex, $K_{EB} = 1.0 \times 10^7 \text{ M}^{-1}$. Scatchard plots also gave the binding constant, K_F as determined from the fluorescence titration using Scatchard equation (4).

$$\log(I_o - I) / I = \log K_F + n \log[\text{Q}] \tag{4}$$

where n is the number of binding sites per nucleotide.

Filter effects were applied as described in literature proceures [47], using equation (5) [48].

$$F_{corr} = F_{obs} 10^{(A_{ex} + A_{em})/2} \tag{5}$$

where F_{corr} and F_{obs} are the corrected and observed fluorescence intensities, respectively, caused by quencher/ fluorophore addition in a 1 cm path-length cuvette.

2.8 Biological studies

2.8.1 Cell culture and in vitro **cytotoxicity**

The cytotoxic effects of the complexes were tested in three human cell lines grown as adherent monolayer cultures, two of which are cancer cell lines (human cervical adenocarcinoma cell line, HeLa, and human foetal lung cancer cell line, MRC5-SV2), while the third one is a normal cell line (human foetal lung fibroblast cell line, MRC5 - the parental line from which the MRC5-SV2 cell line was derived). This combination enabled us to assess the differences in the sensitivies of cancer cell lines to the complexes, as well as the differences in the sensitivies of a cancer cell line and its normal (healthy) parental line, in order to determine the potential cancer cell-selective toxicity of the complexes. Experiments were conducted as previously reported [33]. Cells were grown in 75cm^2 tissue culture flasks using DMEM supplemented with 10% Foetal Bovine Serum, 2mM L-glutamine and 1% antibiotic-antimycotic solution (containing penicillin, streptomycin and amphotericin B), and incubated at 37 $^\circ$C in a humidified atmosphere of 5% CO_2. To prepare culture plates, the tissue culture flask was rinsed with phosphate-buffered saline (PBS), trypsinised, and the cells were suspended in the growth medium. Cell

density was determined by the use of a haemocytometer and adjusted to 7.5×10^4 cells/ml, and 100µl of the suspension (7500 cells) was seeded into each well of a micro-clear, flat-bottom 96-well plates. Seeded plates were incubated for 24 h before the cultures were treated for up to 48 h with a range of concentrations of each complex or a positive control (cisplatin) prepared in growth medium (stocks were prepared in DMSO (cisplatin was prepared in distilled water), but the final DMSO concentration that cells were exposed to was not more than 0.1%v/v). Each treatment was done in triplicate. Following treatment, viability was assessed using the the (MTT) assay by adding 10µl of a 5mg/ml solution of MTT to each well and incubating the plates for 3 h. The content of each well was then aspirated and 100µl of DMSO was added to dissolve the insoluble formazan. Absorbance at 570 nm was then read on a CLARIOstar plate reader (BMG LABTECH, Germany). The mean of triplicate values for each treatment was determined and expressed relative to the mean of the triplicate negative control wells that was set to 100%. An Olympus CKX41 microscope fitted with an Olympus DP71 U-TVIX-2 camera was used to assess and image treatment-induced changes to the morphology of cells. The images were captured with the Olympus cellSens entry software.

2.8.2 Assessment of intracellular levels of reactive oxygen species (ROS)

Changes to intracellular levels of reactive oxygen species (ROS) induced by cisplatin and the complexes in HeLa cells were assessed using the 2',7' – dichlorofluorescin diacetate (DCFDA) Cellular ROS Detection Assay Kit (Abcam, Cat. No. ab113851). Experiments were conducted according to the manufacturer's protocol. HeLa cells were seeded into black, clear bottom 96-well plates at a density of 2.5×10^5 cells/ml (25,000 cells per well) and incubated overnight at 37 °C in a humidified atmosphere of 5% CO_2. The medium was then aspirated from each well and cultures were washed with the buffer solution (1x) supplied with the kit (Abcam) before they were stained for 45 min with 25µM of the DFCDA solution at 100µl/well, with non-stained and blank controls included. Following the 45 min incubation the stain was removed and cultures were washed with buffer. They were then treated with the compounds which had been diluted to the desired concentrations using the full growth medium that contained no phenol red. Cells were then incubated and the fluorescence (Ex/Em = 485/535 nm) of the plate was read at 3 h and at

24 h after treatment on a CLARIO star plate reader. Treatments were done in duplicates and each experiment was repeated at least three independent times. Data were analysed by setting the fluorescence of the negative control (no compound, vehicle only) to '1' (unity) and then calculating the fold change in fluorescence of each treatment compared to the negative control.

2.8.3 Assessment of mechanisms of cell death

Pharmacological assessment of the potential apoptotic or necrotic nature of the cell death elicited by the most promising complex (**PdL₁**) and cisplatin was conducted in HeLa cells using Z-VAD-fmk, a pan-caspase inhibitor (caspases are involved in certain forms of apoptosis), and DPQ, an inhibitor of the nuclear enzyme poly (ADP-ribose) polymerase (PARP), which mediates parthanatos, a form of programmed necrosis. HeLa cells were prepared as reported earlier for cytotoxicity studies. The cultures were pre-treated with Z-VAD-fmk or DPQ for 1 h, after which they were treated with cisplatin or **PdL₁** in the continued presence of each inhibitor. Treatments lasted for 48 h, after which MTT was used to assess viability as previously described in this paper.

2.8.4 Data presentation and statistical analyses

Values are expressed as Mean ± SEM (standard error of the mean) or as otherwise stated. GraphPad Prism (Version 8.3.0) (GraphPad Software, Inc., CA, USA) was used for statistical analyses and the assessment of significant differences between means was done using analysis of variance (ANOVA) followed by a post-hoc test for multiple comparisons (Tukey test), with a p-value of less than 0.05 considered statistically significant. The IC_{50} value for each compound was also determined using GraphPad Prism by fitting the data to the non-linear regression "log [inhibitor] versus normalised response" or "log [inhibitor] versus response (three parameters)," as appropriate. To calculate the Selectivity Index (SI) for each compound, the IC_{50} value for its cytotoxic effect in the normal cell MRC5 was divided by the IC_{50} value for its cytotoxic effect in the cancer variant MRC5-SV2.

3. Results and discussion

3.1. Syntheses and characterisation of the compounds

Ligands **L₁**-**L₃** were synthesised in good yields by the condensation reactions of pyridine-2,6-dicarboxylic acid with the corresponding aniline derivatives following literature procedures [34]. On the other hand, **L₄** was synthesised in good yields (79%) by reactions of *o*-phenylenediamine with iminodiacetic acid according to the synthetic procedure reported by Kopel *et al* [35], (Scheme 1). Complexes **PdL₁**-**PdL₃** were afforded by the treatment of equimolar amounts of **L₁**-**L₄** with PdCl₂(NCMe)₂ in the presence of NaBF₄ in CH₂Cl₂ at room temperature. On the other hand, **PdL₄** was obtained by the reaction of **L₄** with PdCl₂(NCMe)₂ in a 1:1 mole ratio in dichloromethane at room temperature (Scheme 1).
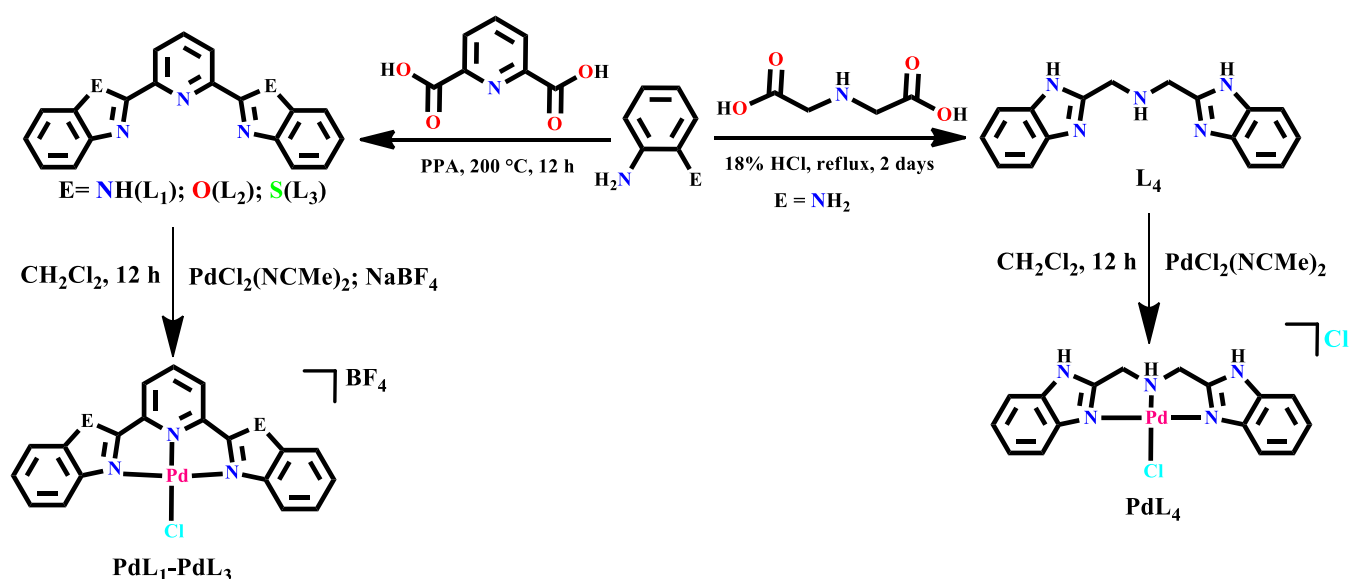
Scheme 1: Synthesis of 2,6-bis(benzazole) ligands **L₁**-**L₄** and corresponding Pd(II) complexes **PdL₁**-**PdL₄**.

The identities of **PdL₁**-**PdL₄** were established by a combination of ^{1}H and ^{13}C NMR (Figures S2-S9), FT-IR spectroscopies (Figures S10-S13), mass spectrometry (Figures S14-S17), elemental analyses and single crystal x-ray analyses. Comparison of ^{1}H and ^{13}C NMR spectra and FT-IR spectra of ligands **L₁**-**L₄** to the spectra of their corresponding Pd(II) complexes **PdL₁**-**PdL₄** established their formation and identities. For example, ^{1}H NMR spectra of **PdL₄** showed two doublets for the two CH₂ linker protons at 4.46 ppm and 4.96 ppm compared to the singlet peak, 4.03 ppm, in the respective ligand **L₄** (Figure S1). The appearance of two doublets of the CH₂ signals in **PdL₄** has been reported and is associated with increased rigidity (resulting in the existence of chair and boat conformations) in the complex relative to a

13

more fluxional behaviour in the free ligand [49]. In the ^{13}C NMR spectral data, the signature carbon peak of the CH_2 group of **PdL$_4$** was observed at 51.39 ppm compared to the peak at 46.48 ppm in the respective ligand. In the IR spectral data, a shift of the absorption band of the υ(N-H) at 2877 cm^{-1} in **L$_4$** to 3104 cm^{-1} in **PdL$_4$** (Figure S13) was observed and confirmed the formation of the complex [50]. Mass spectrometry also proved useful in the elucidation of the molecular formulae of the complexes. For example, the mass spectrum of **PdL$_4$** showed peaks at m/z (%) = 417 [M, 100]$^+$, 838 [M, 12]$^+$ which corresponds to the molecular ion of the complex (Figure S17).

3.2. X-ray molecular structure of complex PdL$_2$ and PdL$_4$

Single crystal suitable for X-ray analyses of **PdL$_2$** and **PdL$_4$** were obtained by slow diffusion of diethyl ether into concentrated solutions of the complexes in CH_3CN and DMSO, respectively at room temperature. Table S1 contains crystallographic data and structural refinement parameters, while Figures. 1 and 2 show the molecular structures and selected bond parameters of complexes **PdL$_2$** and **PdL$_4$**, respectively.

Figure 1: Molecular structure of **PdL$_2$**, with atom numbering Scheme. The displacement ellipsoids of atoms are shown at the 50% probability level. The BF$_4^-$ counter-anion has been omitted for clarity. Selected bond lengths [Å]: Pd(1)-N(3), 2.024(19); Pd(1)-N(1), 2.017(18); Pd(1)-N(2), 1.968(17); Pd(1)-Cl(1), 2.284(5). Selected bond angles (°): N(3)-Pd(1)-N(1), 160.04(7); N(3)-Pd(1)-N(2), 80.09(7); N(1)-Pd(1)-N(2), 79.94(7); N(3)-Pd(1)-Cl(1), 99.80(5); N(1)-Pd(1)-Cl(1), 100.16(5); N(2)-Pd(1)-Cl(1), 179.15(5).
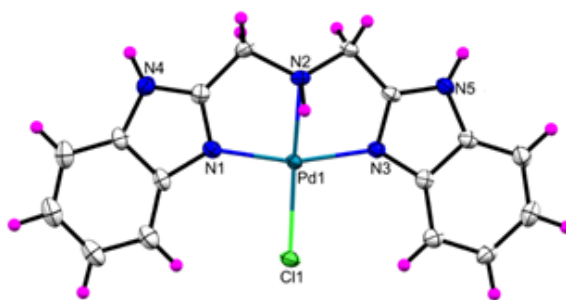
Figure 2: Molecular structure of **PdL₄**, with atom numbering Scheme. The displacement ellipsoids of atoms are shown at the 50% probability level. Selected bond lengths [Å]: Pd(1)-N(3), 2.011(3) ; Pd(1)-N(1), 2.019(3); Pd(1)-N(2), 2.037(3); Pd(1)-Cl(1), 2.308(8). Selected bond angles [°]: N(3)-Pd(1)-N(1), 163.79(10); N(3)-Pd(1)-N(2), 82.59(10); N(1)-Pd(1)-N(2), 81.97(11); N(3)-Pd(1)-Cl(1), 98.05(7); N(1)-Pd(1)-Cl(1), 97.87(7); N(2)-Pd(1)-Cl(1), 173.20(9).

In both structures, the coordination around the Pd metal centre consists of one tridentate ligand and one chloride ligand to give four-coordination environments. The *cis* angles, for instance N1-Pd1-N2 of 79.94(7)° (**PdL₂**) and 81.97(11)° (**PdL₄**) deviate from the ideal 90°. This is also reflected in the *trans* angles, of N2–Pd1–Cl1 of 179.15(5)° for **PdL₂** and 173.20(9)° for **PdL₄** which deviate somewhat from the linearity. Thus, **PdL₂** and **PdL₄**, adopt slightly distorted square planar geometries, consistent for d⁸ Pd(II) complexes [51]. The five membered chelate ring, N(1)-Pd(1)-N(2) of 79.94(7) ° in complex **PdL₂** is smaller than the angle in complex **PdL₄**, for N(1)-Pd(1)-N(2) of 81.97(11).° This can be assigned to the the rigid pyridine ring, when compared to the more flexible CH₂ linker in **PdL₁** and **PdL₄** respectively.

The bond distances Pd(1)-N(3) of 2.024(19) Å and Pd(1)-N(3) of 2.011(3) Å in **PdL₂** and **PdL₄**, respectively, are statistically similar, presumably due to the remote proximity of the heteroatoms to the palladium metal centre. A similar trend is observed in the bond lengths for Pd(1)-N(1) of 2.017(18) Å and 2.019(3) Å for **PdL₂** and **PdL₄** respectively. The shorter bond length for Pd(1)-Cl(1) of 2.284(5) Å in complex **PdL₂** compared to the Pd(1)-Cl(1) bond distance of 2.308(8) Å in **PdL₄** may be attributed to the aromatic pyridine ring in **L₂**, which is a pi-acceptor (less *trans*-effect) in comparsion to the sigma-donor N-H group in **L₄**. The Pd-Cl bond lengths of 2.284 (5) Å for **PdL₂** is within the average bond distance of 2.289 Å obtained for 20 related Pd complexes. Similarly, the Pd-Cl bond length of 2.308(8) Å in **PdL₄** falls within the average bond distance of 2.327 ± 0.017 Å reported for 19 similar structures [52]. The

Pd(1)-N$_{py}$ bond distance for **PdL$_2$** of 1.968(17) Å agrees well with the averaged bond lengths of 1.950 ±

0.039 Å reported in 15 structures. Likewise, the bond distance of Pd-Nim of 2.037 (3) is comparable to

the bond distance of Å 2.048 ± 0.025 Å (**PdL$_4$**), averaged for 16 related structures [40]. The mean bond

distances of Pd–N(1&3) of 2.021(19) Å and 2.015(3) Å for **PdL$_2$**, and **PdL$_4$**, compare well with the

averages of 2.025 ± 0.031Å (16 structures) and 1.980 ± 0.053 (15 structures) obtained for similar

complexes respectively [53].

3.4 Kinetic and mechanistic measurements with biomolecules

The rate of the displacement of the coordinated chloro ligand from the four complexes was studied

with three biologically-relevant nucleophiles: Tu, L-Met and 5'-GMP, under *pseudo*-first order conditions.

Representative plots of k_{obs} versus the concentration of the entering ligand, [Nu], for **PdL$_1$** is given in

Figure 3; similar plots for **PdL$_2$**-**PdL$_4$** are presented in the supporting information (Figure S18-S20). The

second order rate constants (k_2) were derived from the slopes of the graphs and are given in Table 1. Since

the zero y-intercept were observed in all the plots, the relationship between k_{obs} and the concentration of

the entering ligand can be best described by equation (6).

$$k_{obs} = k_2[\text{Nu}] \tag{6}$$
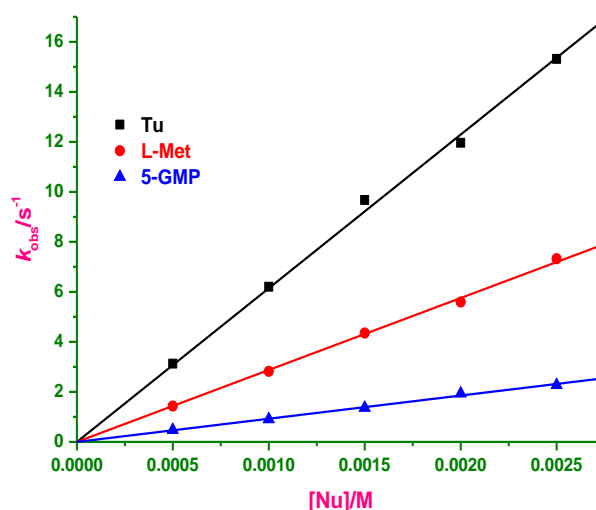
Figure 3: Dependence of k_{obs} on the nucleophile concentration for chloride substitution from **PdL$_1$** at T =

298 K in aqueous solution, 25mM Hepes buffer (pH =7.2) and 10 mM NaCl.

Comparing the rates of the substitution of the chloride ligands from the complexes by incoming nucleophiles, the reactivity decreases in the order **PdL₁** > **PdL₂** > **PdL₃** > **PdL₄** (refer Table 1). The marked differences in the observed reactivity can be rationalised in terms of the presence of electronic interactions between inert tridentate ligands and Pd(II) metal centre. Significantly, the reactivity of **PdL₁-PdL₃** are controlled by the identity of the heteroatoms on the spectator ligands(s) around the metal centres. The higher reactivity of **PdL₁** (N-H), 6146 $M^{-1}s^{-1}$ (**Tu**), than **PdL₂** (O), 5433 $M^{-1}s^{-1}$ (**Tu**) and **PdL₃** (S), 3908 $M^{-1}s^{-1}$ (**Tu**) is attributable to the presence of the acidic amine proton, which is more electron deficient and thus aids the withdrawal of the electrons from the metal centre and hence creating a more electrophilic Pd(II) metal centre. A comparison of the reactivity of **PdL₂** and **PdL₃** shows that, **PdL₂** is more reactive due to the presence of a more electronegative oxygen on the spectator ligand [33]. With respect to the solid-state structure of complexes **PdL₂** and **PdL₄**, one would expect a higher rate of substitution of the Cl ligand in **PdL₄** due its longer Pd - Cl bond (2.308 (8) Å) in comparison to complex **PdL₂** (Pd - Cl = 2.284 (5) Å). In contrast, the higher reactivity of complex **PdL₂** thus implicates nucleophilic attack to the Pd atom as the rate determining step, rather than Pd-Cl breakage, consistent with an associated mode of substitution reactions.

In order to verify the observed reativity trend of the Pd complexes, we performed DFT calcuations to determine the electronic and steric properties of the respective compounds (Tables S2 and S3). The observed kinetics trend is supported by the DFT data indicating the decrease in the negative NBO charges of the heteroatoms from **PdL₁** to **PdL₃**, leading to a decrease in the removal of electron density from the Pd(II) ion. This is also supported by the electrophilicity indices (ω, see Table S3) of the complexes which corroborates with the reactivity. In addition, the chemical hardness and electrochemical potentials are also in line with the experimental reactivity trend of the complexes. Similarly, it is also clear that **PdL₁** is ≈ 45 times more reactive than **PdL₄**. The enhanced reactivity of **PdL₁** in relation to **PdL₄** may be attributed to the effective π back-bonding of the in-plane-coordinated pyridine moiety with non-bonding *d*-electrons that increase electrophilicity of the metal ion [32, 54]. The enhanced π-acceptor ability of **PdL₁**, compared to **PdL₄**, is further evidenced by the high electrophilicity index of **PdL₁** than **PdL₄** (Table S3). Further,

the non-planar geometry of **PdL₄** in comparison to **PdL₁**- **PdL₃** (Table S2) offers a slight steric hindrance between the ipso-hydrogen and the incoming nucleophile, thus lowering its reactivity. In addition, DFT computations support the role of the π-back donation of the pyridyl moiety from the dipole moments of 15.5524 and 11.0864 for **PdL₁** and **PdL₄**, respectively (Table S3). Likewise, the diminution of the HOMO-LUMO energy separation of complexes at ground state [55], illustrates an upward trend as one moves from **PdL₁** to **PdL₄**, thus confirming the more stable nature of **PdL₄** than the other complexes. Overall, DFT calculated data shows higher ionisation potential, high chemical hardness, and smaller $\Delta E_{LUMO–HOMO}$ values for complex **PdL₄** compared to the other complexes.

With respect to the incoming biological nucleophile, the reactivity of the three nucleophiles follows the order; **Tu** > **L-Met** > **5'-GMP** (Table 1). **Tu** is relatively less sterically demanding in comparisons to **L-Met** > **5'-GMP** nucleophiles (Figure 4). The higher reactivity of **L-Met** than **5'-GMP**, can be explained by the presence of sulfur donor atom, which is known to have a higher affinity for soft Pd(II) cation than the nitrogen atom [56]. Notably, lower reactivity exhibited by 5′-GMP nucleophile, may be ascribed to the presence of the N-donor atom and the steric bulk of the 5′-GMP.
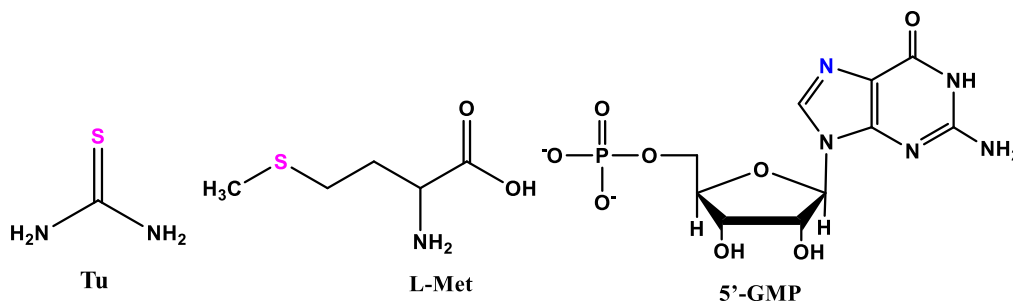
Figure 4: Molecuar structures of the investigated biological nucleophiles.

To determine the thermodynamic properties of the substitution process, the reaction temperature was varied from 298 to 328 K at an interval of 10 K. Activation parameters ($\Delta H^{\neq}$ and $\Delta S^{\neq}$) were calculated using the Eyring equation [26]. Typical Eyring plots obtained for complex **PdL₁** are shown in Figure 5 and the values of $\Delta H^{\neq}$ and $\Delta S^{\neq}$ are given in Table 1. The Eyring plots and values for the other three complexes **PdL₂**-**PdL₄** are presented in the supporting information (Figures S21-S23). For all the investigated complexes, the activation enthalpies ($\Delta H^{\neq}$) and entropies ($\Delta S^{\neq}$) were positive and negative, respectively. The large sensitivity of the rate constants for the σ-donor properties of the nucleophiles is in

18

tandem with an associative mode of substitution [56]. Furthermore, the activation parameters, ($\Delta H^{\neq} > 0$, $\Delta S^{\neq} < 0$) support an associative mechanism, in agreement with square-planar d^8 metal complexes [57, 58].
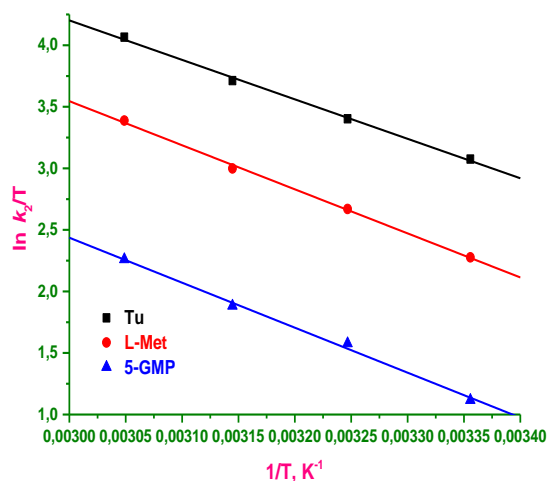
Figure 5: Eyring plots for the reaction of **PdL₁** with the nucleophile in aqueous solution, 25 mM Hepes buffer (pH =7.2) and 10 mM NaCl.

Table 1: Summary of the second order rate constants, k_2 and activation parameters, $\Delta H^{\neq}$ and $\Delta S^{\neq}$ for the substitution reactions of complexes **PdL₁-PdL₄** by **Tu**, **L-Met** and **5-GMP**.ᵃ

Complex	Nu	k_2/M⁻¹ s⁻¹	$\Delta H^{\neq}$/ kJ mol⁻¹	$\Delta S^{\neq}$/J mol⁻¹K⁻¹
	Tu	6146 ± 78	27 ± 1.0	-83 ± 3.0
PdL₁	**L-Met**	2877 ± 28	30 ± 1.0	-79 ± 3.0
	5-GMP	927 ± 13	30 ± 1.4	-86 ± 4.4
	Tu	5433 ± 41	33 ± 2.5	-62 ± 8.0
PdL₂	**L-Met**	2072 ± 18	35 ± 1.0	-62 ± 3.0
	5-GMP	830 ± 3	33 ± 2.2	-78 ± 7.0
	Tu	3908 ± 30	32 ± 0.3	-69 ± 1.0
PdL₃	**L-Met**	1363 ± 17	34 ± 0.3	-72 ± 1.0
	5-GMP	599 ± 4	37 ± 1.0	-68 ± 3.3
	Tu	1072 ± 9	34 ± 1.3	-73 ± 4.2

PdL4	L-Met	486 ± 3	33 ± 1.0	-85 ± 3.3
	5-GMP	178 ± 3	34 ± 1.0	-90 ± 3.1

[a]Reactions performed in aqueous solution, 25mM Hepes buffer (pH =7.2) and 10 mM NaCl at 298 K.

3.5 CT-DNA interactions

3.5.1 UV-visible absorption measurement

The interactions between metal complexes and duplex CT-DNA were monitored by following the changes in the absorbance upon addition of CT-DNA to a fixed concentration of the Pd(II) complex. Typical graphs are given in Figure 6 (**PdL1**) and Figures S24- S26 (**PdL2 –PdL4**) for the spectral charges due to the Pd – CT-DNA interactions. The spectral titration curves showed a common hypochromic shift with an increase in CT-DNA concentration. The observed hypochromism may be attributed to π–π stacking interaction between the aromatic chromophore of the complexes and DNA base pairs, consistent with intercalative binding mode, while the red-shift was indicative of the stabilisation of the DNA duplex [59]. The binding constants obtained in this study of between 0.2 x 10^5 and 5.0 x 10^6 M^{-1} are comparable to those obtained for other metal complexes [59-64]. The higher DNA binding of **PdL1**, **PdL2** and **PdL3** may be assigned to the planarity of the complexes, consistent with the DFT calculations. The K_b values of **PdL1**-**PdL3** are within the classical intercalator EB binding affinity for CT-DNA of $K_{b,}$ = 1.4 x 10^6 M^{-1} [65].
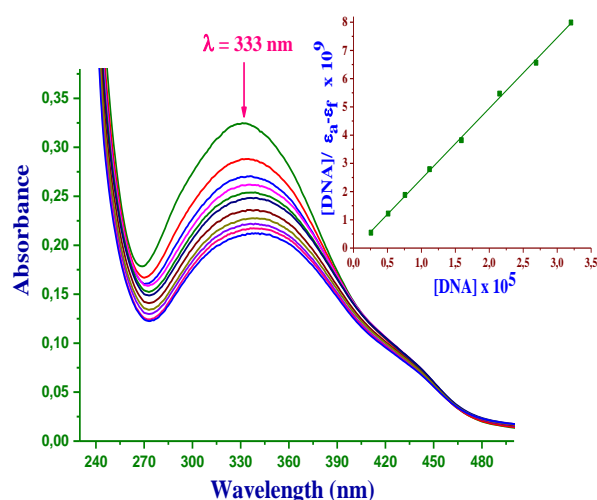
Figure 6: Absorption spectra of **PdL₁** complex (20 µM) in Tris-HCl/50 mM buffer at pH 7.2 upon addition of CT-DNA (0 - 40 µM). The arrow shows the change in absorbance upon increasing the CT-DNA concentration. Inset: plot of [CT-DNA] versus $[DNA]/(\varepsilon_a - \varepsilon_f)$.

3.5.2 Competitive CT-DNA-EB binding studies

To further support the interaction mode of the complexes with DNA, competitive binding studies were performed by following the quenching of the fluorescence emission intensity of CT-DNA-EB complex after each addition of the Pd(II) complex. In all cases, the intensity of emission was quenched with a notable red shift of λ_{max} (Figures 7, S27 - S29). These point to the existence of strong interactions between Pd(II) complexes and CT-DNA. The quenching data were fitted to the Stern-Volmer equation which gave linear Stern-Volmer quenching constant, K_{sv}. Typical Stern-Volmer plot for the reaction between **PdL₁** and CT-DNA is given in Figure 7a. The K_{sv} values of **PdL₁-PdL₄** ($\sim 10^4$ M^{-1}), suggest that the complexes efficiently replaced EB through intercalative binding to CT-DNA (Table 2) [59]. The values of apparent binding constant, K_{app}, (Table 2) followed the same trend observed for K_{sv} values.

Table 2: The binding constants and quenching constants for **PdL₁-PdL₄** complexes with CT-DNA

Complex	UV titration	EB fluorescence exchange titration				
	K_b x 10⁶, M^{-1}	K_{sv} x 10⁴, M^{-1}	K_{app} x 10⁶, M^{-1}	k_q x 10¹², M^{-1} s^{-1}	K_F x 10⁵, M^{-1}	n
PdL₁	5.53	5.43 ± 0.21	2.96 ± 0.19	2.36 ± 0.27	16.59 ± 0.13	1.34
PdL₂	2.20	2.84 ± 0.17	1.07 ± 0.15	1.24 ± 0.21	6.88 ± 0.10	1.39
PdL₃	1.01	1.92 ± 0.13	0.80 ± 0.09	0.84 ± 0.14	0.44 ± 0.08	1.00
PdL₄	0.53	0.54 ± 0.08	0.16 ± 0.03	0.23 ± 0.10	0.09 ± 0.19	1.17

Intrinsic binding constant, K_b is given in M^{-1}; stern-volmer quenching constant, K_{sv} expressed in M^{-1}; apparent binding constant, K_{app} given in M^{-1}; bimolecular quenching rate constant, k_q provided in M^{-1}s^{-1} binding constant, K_F presented in M^{-1}; and number of DNA binding sites, n.

The values of bimolecular quenching rate constant, k_q, were also computed using the $K_{SV} = k_q\tau_0$ and recorded in the order of $\sim 10^{12}$ M^{-1} s^{-1} and followed the trend of **PdL₁** > **PdL₂** > **PdL₃** > **PdL₄** (Table

2). These values are higher than the known strong biopolymer fluorescence quenchers (10^{10} M^{-1} s^{-1}), and thus it can be deduced that the complexes quench EB fluorescence statically rather than dynamically [66]. The Scatchard equation, $\log(I_o - I) / I = \log K_F + n \log[Q]$ was used to determine the number of binding site, n and binding constant, K_F (Table 2). Linear plots of **PdL1** is given in Figure 7, while supporting Figures S27-S29 represent plots for complexes **PdL2** – **PdL4** respectively. The n values obtained for all the complexes were approximately equal to 1, demonstrating that the complexes bind to CT-DNA in a 1:1 mole ratio. EB, which shows a K_F of $\sim 10^5$ M^{-1}, was assumed to occupy more than one DNA binding site [67]. The magnitude of the binding constants and quenching rate constants decrease according to the ability of the complexes to displace EB of the base pairs and followed the trend **PdL1** > **PdL2** > **PdL3** > **PdL4**. Complex **PdL4** displayd the lowest binding affinity, consistent with the DNA binding data described *vide supra*.
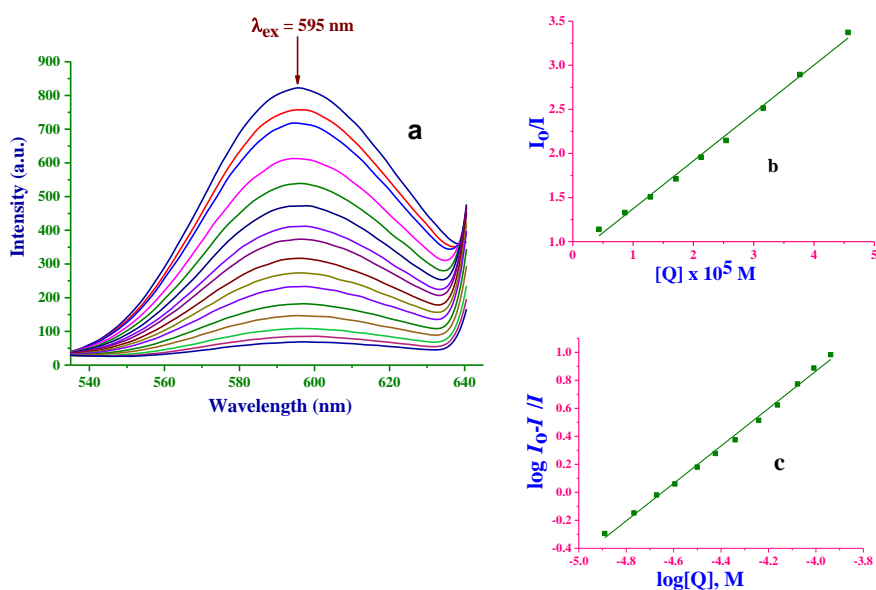
Figure 7: (**a**); Fluorescence emission spectra of EB bounded to CT-DNA in the presence of **PdL1**: [EB] = 6.5 μM, [CTDNA] = 6.5 μM and [**PdL1**] = 0-200 μM. The arrow shows the intensity changes upon increasing the **PdL1** complex concentration. (**b**); Stern-Volmer plot of I_o/I versus [Q]. (**c**); Scatchard plot of $\log[(I_o–I)/I]$ versus $\log[Q]$.

3.6 Molecular docking with B-DNA

To further elucidate the observed spectroscopic binding trends of **PdL₁-PdL₄**, molecular docking simulations were performed to determine the minimum energy of DNA-complex structure and the preferred binding site and best orientation of the complexes within the DNA groove. The complexes were docked onto B-DNA and the minimum energy of the docked poses for **PdL₁-PdL₄** revealed that the complexes fitted into the curved contours of the B-DNA located in the G–C (~13.4 Å) bases sequence (Figure S30). The minimised free energies of the docked structures of complexes **PdL₁**, **PdL₂**, **PdL₃**, and **PdL₄** were found to be -270.07, -268.81, -266.11 and -263.96 kJ mol^{-1}, respectively (Figure S30). The observation is consistent with the DNA binding propensity of the complexes (Table 2).

3.7 Cytotoxic activities of cisplatin and the complexes PdL₁-PdL₄ against HeLa, MRC5-SV2 and MRC5 cells

The cytotoxicities of Pd(II) complexes and cisplatin (used as a reference drug) were investigated in two malignant cell lines (HeLa, MRC5-SV2) and in a healthy cell line (MRC5) using the MTT assay, following up to 48 h of treatment. Figure 8 shows the effects of complexes **PdL₁-PdL₄** and cisplatin on the viability of HeLa, MRC5-SV2 and MRC5 cells, while Figure S31 depicts morphological damage to each of the cell lines, using cisplatin as the standard drug control. Cisplatin and the complexes (6.25 – 100 µM) each reduced the viability of each of the three cell lines in a concentration-dependent manner (Figure 8). In addition, we confirmed that the effects of both cisplatin and **PdL₁** were also time-dependent, as the reductions in viability at 48 h were significantly higher than at 24 h (Figure 8a and 8c). In fact, at 25, 50 and 100 µM concentrations, both cisplatin and **PdL₁** revealed profound differences between their toxic effects at 24 h and at 48 h, with toxic effects (indicated by reduction in viability) at 48 h almost double or triple those at 24 h. The three cell lines exhibited differential sensitivities to cisplatin and the Pd(II) complexes. Based on the calculated IC$_{50}$ values (Table 3), cisplatin was equipotent (IC$_{50}$ of 11.4µM) in its toxicity against the cancer cells lines HeLa and MRC5-SV2, while it was less cytotoxic against the normal cell line MRC5. The IC$_{50}$ of **PdL₁** for the HeLa cells (16.3 ± 4.9) was not statistically significantly different from that of cisplatin, demonstrating the equipotency of **PdL₁** and cisplatin against the HeLa cell.

However, all the four complexes were less potent than cisplatin against the MRC5-SV2 cell, with **PdL₁** being twice less potent than cisplatin. **PdL₂**, **PdL₃** and **PdL₄** were each much less potent than **PdL₁** or cisplatin against the HeLa cell (four-, five- and nearly 5-fold less potent, respectively, compared to **PdL₁**), whereas **PdL₂** and **PdL₃** were almost equipotent with **PdL₁** against the MRC5-SV2 cell, and **PdL₄** was only one-and-a-half times less potent than **PdL₁** against the MRC5-SV2 cell. The orders of potencies against HeLa and MRC5-SV2 cells, respectively, are **PdL₁** > **PdL₂** > **PdL₄** > **PdL₃** and **PdL₃** > **PdL₂** > **PdL₁** > **PdL₄**.
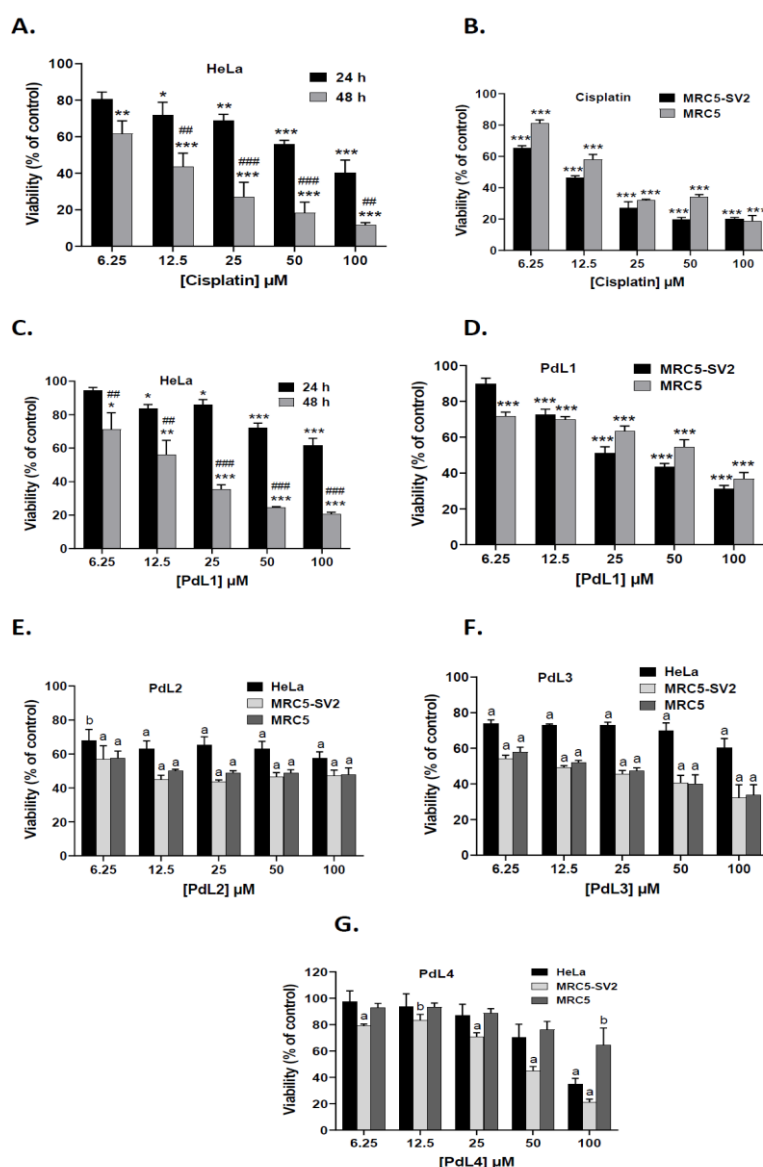
Figure 8: Effects of complexes **PdL₁**-**PdL₄** and cisplatin on the viability of HeLa, MRC5-SV2 and MRC5 cells. (a) Concentration-dependent effects of cisplatin on HeLa cell viability. (b) Effects of 48 h treatment with cisplatin on the viability of MRC5-SV2 and MRC5 cells. (c) Concentration-dependent effects of **PdL₁** on HeLa cell viability. (d) Effects of 48 h treatment with **PdL₁** on the viability of MRC5-SV2 and

MRC5 cells. (e) Effects of 48 h treatment with **PdL₂** on the viability of HeLa, MRC5-SV2 and MRC5 cells. (f) Effects of 48 h treatment with **PdL₃** on the viability of HeLa, MRC5-SV2 and MRC5 cells. (g) Effects of 48 h treatment with **PdL₄** on the viability of HeLa, MRC5-SV2 and MRC5 cells. Each value is expressed as Mean ± SEM of 3 or 4 independent experiments. *$P<0.05$, **$P<0.01$ (or ^{b}$P<0.01$) and ***$P<0.001$ (or ^{a}$P<0.001$) compared to the negative control; ##$P<0.01$ and ###$P<0.001$ for the comparison of the effects at 24 h and 48 h.

Overall, **PdL₄** exhibited the least cytotoxic effects on the tumour cell lines (not much different to **PdL₂** or **PdL₃** in its effect against HeLa, but about twice less potent than **PdL₁**-**PdL₃** against MRC5-SV2). The presence of the pyridyl rings in **PdL₁**-**PdL₃** is thought to increase the hydrophobicity of the **PdL₁**-**PdL₃** complexes and could have eased their passage through the cell membrane to allow more complexes into the cells [68]. However, the reduced toxicity of **PdL₄** suggests that the removal of a pyridine ring (reduced number of conjugation) on the inert ligand architecture leads to a decrease in cytotoxic (anti-tumour) activity [69]. The lower cytotoxic activity of **PdL₄** could also be due to the steric hindrance caused by methylene moiety, as illustrated by the planarity diagram in DFT (Table S2) and lower DNA binding constants (Table 3). The minimal cytotoxicity of **PdL₄** could also be attributed to its slower ligand exchange kinetic behaviour, since the complex was the least reactive as per the kinetics data in Table 1 [33].

As a major goal in chemotherapy is to selectively target cancer cells while relatively sparing normal cells, we assessed the cancer-cell selectivity of cisplatin and the complexes, based on the Selectivity Index (SI) parameter. As shown in Table 3, both cisplatin and **PdL₁** had similar SI values of 1.6 and 1.5, respectively, which depicts that they are almost twice as potent in killing cancer cells as they are in killing normal cells. Of all compounds tested, **PdL₄** had the highest SI (2.4), which could be attributed to its low potency in general. On the other hand, both **PdL₂** and **PdL₃** yielded very low SI values (1.2 and 1.1, respectively), suggesting that they had little selectivity for cancer cells over normal cells and are thus, in drug discovery context, not optimal in their current forms for therapeutic applications. In general, among the Pd(II) complexes investigated, the effects of the complexes on cell viability and their cancer-cell selectivities reveal **PdL₁** as the most promising compound.

Table 3: Cytotoxic potencies and cancer-cell selectivities of cisplatin and **PdL$_1$-PdL$_4$**

	IC$_{50}$ (μM)			
	HeLa	**MRC5-SV2**	**MRC5**	**Selectivity Index (SI)**
Cisplatin	11.4 ± 3.5	11.4 ± 0.5	18.7 ± 1.3	1.6
PdL$_1$	16.3 ± 4.9	25.0 ± 0.3	37.3 ± 0.2	1.5
PdL$_2$	70.3 ± 16.6	21.1 ± 4.0	26.1 ± 3.3	1.2
PdL$_3$	88.4 ± 21.5	18.5 ± 2.6	20.5 ± 1.9	1.1
PdL$_4$	73.6 ± 7.0	39.8 ± 3.4	96.8 ± 0.7	2.4

IC$_{50}$ values, rank orders of cytotoxic potencies and selectivity indices (SI) for cisplatin (as the standard) and **PdL$_1$-PdL$_4$** against two cancer cell lines (HeLa and MRC5-SV2 cells) and a normal (healthy) cell line (MRC5) that is parental to the MRC5-SV2 cell. SI is calculated as a ratio of the IC$_{50}$ for the compound against the normal cell line (MRC5) and its IC$_{50}$ against the cancer cell line (MRC5-SV2). Each IC$_{50}$ value is expressed as Mean ± SEM.

3.7.1 ROS generation as potential mechanism for the cytotoxicity of complexes

Cytotoxic and chemotherapeutic compounds could engage a variety of mechanisms to induce their cytotoxicity in cancer and normal cells, including the generation of significant levels of reactive oxygen species (ROS) within the cell [70]. The ROS could trigger a host of downstream toxic responses culminating in cell death, including damage to lipids, proteins and DNA [71]. For example, cisplatin chemotherapy generates oxidative stress in normal cells, which is responsible for its non-specific toxicity. We, therefore, explored, using HeLa cells, whether the complexes could induce significant ROS levels intracellularly. Interestingly, contrary to previous reports [72], we did not find any evidence within our experimental system that the reduction in cell viability (toxicity) induced by cisplatin was dependent on its generation of a significant level of ROS (Table 4), as the ROS levels at 3 h and 24 h following treatment with cisplatin up to 100 μM were not different from the basal ROS level (Table 4). This suggests that cisplatin's toxicity could depend on contributions from ROS-dependent and independent processes, a phenomenon which could depend on other factors including the cellular environment. Similarly, **PdL$_1$** did not initially have any effect on basal ROS level (3 h) but decreased (at 25 μM and 100 μM) basal ROS level at 24 h (Table 4), a time point at which it had begun to elicit moderate but significant toxic effects,

thus presenting a conundrum. We opine that, for **PdL₁**, cytotoxic mechanisms other than raised levels of ROS might operate in a much greater proportion that overwhelms any beneficial and, perhaps, transient anti-ROS effect induced by **PdL₁**, thus resulting in a net toxic effect.

PdL₂ and **PdL₄** did not have any significant effect on intracellular ROS levels. While **PdL₃** was five times less potent than **PdL₁** in its toxicity against the HeLa cell, it was the only complex that induced a significant increase in intracellular ROS. At 100 μM, **PdL₃** increased ROS level significantly and relatively quite early on in the treatment (3 h), nearly doubling ROS level compared to the basal (control) level, an effect that was sustained up to the much later 24 h time point. This clearly indicates that the generation of ROS contributes to the cytotoxicity of **PdL₃**, unlike was the case for the other complexes. We, therefore, on the basis of ROS, identified the four complexes as belonging to two mechanistic groups: one which induces cytotoxicity through ROS, and the other whose cytotoxicity is rather ROS-independent.

Table 4: Changes to intracellular ROS levels induced by cisplatin and **PdL₁-PdL₄**

	Intracellular Reactive Oxygen Species (ROS) levels (fold change vs. control)					
	3 h			24 h		
	6.25μM	25μM	100μM	6.25μM	25μM	100μM
Cisplatin	1.1 ± 0.1	1.1 ± 0.1	1.1 ± 0.1	0.8 ± 0.1	0.7 ± 0.1	0.7 ± 0.1
PdL1	1.1 ± 0.0	1.0 ± 0.0	1.1 ± 0.1	0.9 ± 0.0	$0.7 \pm 0.0*$	$0.6 \pm 0.0***$
PdL2	1.1 ± 0.1	1.2 ± 0.0	1.2 ± 0.1	1.0 ± 0.0	0.9 ± 0.0	1.1 ± 0.1
PdL3	1.1 ± 0.1	1.4 ± 0.1	$1.8 \pm 0.2*$	1.0 ± 0.0	1.1 ± 0.0	$1.7 \pm 0.2*$
PdL4	1.0 ± 0.0	1.1 ± 0.1	1.3 ± 0.1	0.8 ± 0.1	0.9 ± 0.1	1.1 ± 0.2

Effects of cisplatin and complexes **PdL1-PdL4** on the intracellular levels of reactive oxygen species (ROS) as measured by DCFDA. Following treatment of HeLa cells with the indicated compounds, the fluorescence of DCFDA was read at 3 h and 24 h at an excitation wavelength of 485 nm and an emission wavelength of 535 nm (fluorescein). Values represent Mean ± SEM (n=3 or 4 independent experiments) of fold change in ROS levels (compared to the negative control that was set to unity). Values are rounded up to 1 decimal place. $*P<0.05$, $***P<0.001$ compared to the control.

3.7.2 Nature of cell death induced by cisplatin and PdL₁

Cytotoxic or chemotherapeutic agents induce cellular damage, which could result in one or, more usually, a combination of some of the various forms of cell death, including but not limited to apoptosis and necrosis [73]. We, therefore, investigated the potential proportions of apoptosis or necrosis in the cell death induced by **PdL₁**, the most promising of the complexes, and cisplatin. The cultured HeLa cells were treated with either cisplatin or **PdL₁** in the absence or presence of a chemical inhibitor of apoptosis or necrosis. The inhibitor of apoptosis used, Z-VAD-fmk, blocks caspases, whichmediate apoptosis, while DPQ, an inhibitor of the enzyme poly (ADP-ribose) polymerase (PARP), blocks parthanatos (PARP-1-dependent cell death) [74], now considered a type of programmed necrosis [75]. The results are as presented in Figure 9.
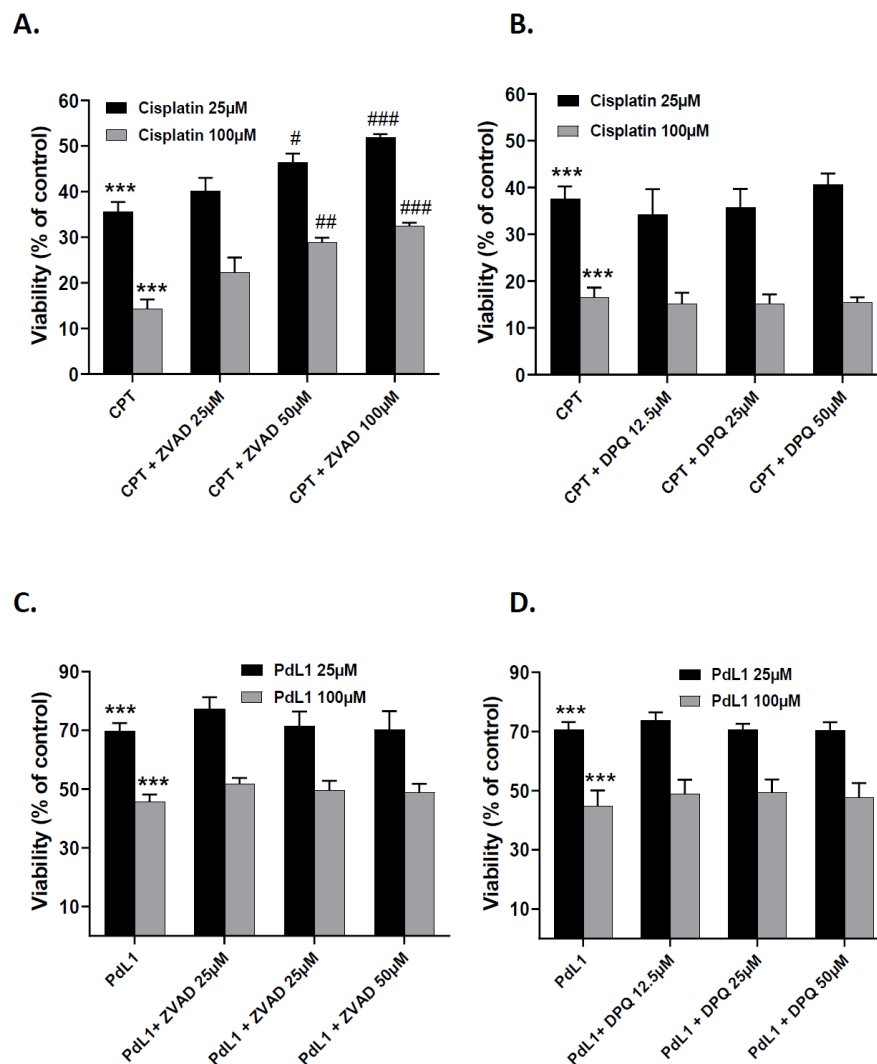
Figure 9: Induction of apoptotic or necrotic cell death by cisplatin (CPT) and **PdL₁** (48 h treatment). (A) Concentration-dependent protective effects of the pan-caspase inhibitor, Z-VAD-fmk (25 -100 μM), against the cytotoxic effect of low (25 μM) and high (100 μM) concentration of cisplatin. (B) Lack of effect of the PARP inhibitor, DPQ (12.5 – 50 μM), against the cytotoxic effect of low (25μM) and high (100 μM) concentration of cisplatin. (C) Lack of effect of the pan-caspase inhibitor, Z-VAD-fmk (25 - 100 μM), against the cytotoxic effect of low (25 μM) and high (100 μM) concentration of **PdL₁**. (D) Lack of effect of the PARP inhibitor, DPQ (12.5 – 50 μM), against the cytotoxic effect of low (25μM) and high (100 μM) concentration of **PdL₁**. Each value is expressed as Mean ± SEM of 3 independent experiments. ***$P < 0.001$ compared to the negative control; #$P < 0.05$, ##$P < 0.01$ and ###$P < 0.001$ compared to CPT alone or **PdL₁** alone.

The cytotoxic effects of cisplatin, whether at a low or a high concentration, were significantly ameliorated by the pan-caspase inhibitor, Z-VAD-fmk, but not affected by the PARP inhibitor DPQ, suggesting that, at least, the cell death induced by cisplatin was significantly apoptotic in nature, with little evidence of necrosis, consistent with earlier reports [76]. On the other hand, the cytotoxic effects of **PdL₁** were not affected by the inhibitors, implying that caspase-dependent apoptosis and PARP-dependent programmed necrosis of parthanatos might not play a significant role in **PdL₁**-induced cell death, at least within the context of our experimental system. The differences both in the cell death mechanisms predominantly engaged by cisplatin and **PdL₁** and in the manner of their inducing changes to, or not affecting, intracellular ROS levels, support the establishment of the fact that cisplatin and **PdL₁** do not share exactly the same mechanisms of action. This could be advantageous in the development of novel metallodrugs that are endowed with toxic mechanisms dissimilar to those of cisplatin.

4. Conclusions

Palladium(II) complexes of tridentate bis(benzazole) ligands have been synthesised and structurally characterised. The solid-state structure of the complexes established a tridentate coordination mode of the ligands to give square planar complexes. The rates of substitution kinetics of the Pd(II) complexes were mainly controlled by the electronic properties of the auxiliary ligands and incoming nucleophile. DFT calculations supported the reactivity trends. The values of activation parameters, $\Delta H^{\neq}$ and $\Delta S^{\neq}$ support an associative mode of activation. The competitive CT-DNA binding affinities are controlled by the steric bulk of the ligands, consistent with molecular docking experiments. Complex **PdL₁** displayed cytotoxic potency and selectivity comparable to those of cisplatin. Only **PdL₃** significantly

increased ROS levels while **PdL₄** was the most cancer cell-selective but the least potent. There was no evidence that **PdL₁** induces significant apoptotic cell death, unlike cisplatin. Complexes **PdL₁** and **PdL₂** showed good correlations on the rates of substitution kinetics, DNA binding affinities and cytotoxicity activities, thus providing evidence on the use of substitution kinetics and DNA binding studies to probe the cytotoxicity of these types of Pd(II) complexes.

Supplementary information

Supplementary materials contain additional NMR and IR spectroscopic spectral data, mass spectra of the palladium complexes and X-ray crystallography files. The CCDC data entries for the structures are CCDC: 1992172 and 1992173 for compounds **PdL₂** and **PdL₄**, respectively. The material also contains additional kinetics plots, DNA binding UV-visible and fluorescence spectra, optimised DFT structures and results, molecular docking diagrams and cell morphology images.

References

[1] S. Dilruba, G.V. Kalayda, Cancer Chemother. Pharmacol. 7 (2016) 1103-1124.

[2] A. Khan, R. Rashid, G. Murtaza, A. Zahra, Trop J Pharm Res. 13 (2014) 1169-1177.

[3] H. Zhao, T. Bi, Z. Qu, J. Jiang, S. Cui, Y. Wang, Oncol Rep. 32 (2014) 1003-1012.

[4] C.J. Jones, J.R. Thornback Journal (2007) Pages.

[5] E. Tiekink, Inflammopharmacology, 16 (2008) 138-142.

[6] G. Gasser, N. Metzler-Nolte, Curr. Opin. Chem. Biol. 16 (2012) 84-91.

[7] E. Alessio Journal (2011) Pages.

[8] J. Yellol, S.A. Pérez, A. Buceta, G. Yellol, A. Donaire, P. Szumlas, P.J. Bednarski, G. Makhloufi, C. Janiak, A. Espinosa, J. Med. Chem. 58 (2015) 7310-7327.

[9] A. Zamora, C.A. Denning, D.K. Heidary, E. Wachter, L.A. Nease, J. Ruiz, E.C. Glazer, Dalton Trans. 46 (2017) 2165-2173.

[10] T. Zou, C.-N. Lok, P.-K. Wan, Z.-F. Zhang, S.-K. Fung, C.-M. Che, Curr. Opin. Chem. Biol. 43 (2018) 30-36.

[11] A.A. Fathy, I.S. Butler, M.A. Elrahman, B.J. Jean-Claude, S.I. Mostafa, Inorg. Chim. Acta. 473 (2018) 44-50.

[12] R. Kanaoujiya, M. Singh, J. Singh, S. Srivastava, J. Sci. Res. 64 (2020).

[13] V. Vidimar, C. Licona, R. Cerón-Camacho, E. Guerin, P. Coliat, A. Venkatasamy, M. Ali, D. Guenot, R. Le Lagadec, A.C. Jung, Cancer Lett. 440 (2019) 145-155.

[14] N. Mirzadeh, T.S. Reddy, S.K. Bhargava, Coord. Chem. Rev. 388 (2019) 343-359.

[15] C.K. Adokoh, RSC Adv. 10 (2020) 2975-2988.

[16] H. Zhang, F. Xie, M. Cheng, F. Peng, J. Med. Chem. 62 (2019) 6985-6991.

[17] L. Noriega, M.E. Castro, J.M. Perez-Aguilar, N.A. Caballero, B.L. Sanchez-Gaytan, E. González-Vergara, F.J. Melendez, J. Inorg. Biochem. 203 (2020) 110862.

[18] H. Mansouri-Torshizi, S. Shahraki, Z.S. Nezami, A. Ghahghaei, S. Najmedini, A. Divsalar, H. Ghaemi, A.-A. Saboury, Complex Metals, 1 (2014) 23-31.

[19] C. Icsel, V.T. Yilmaz, Y. Kaya, H. Samli, W.T. Harrison, O. Buyukgungor, Dalton Trans. 44 (2015) 6880-6895.

[20] K.A. Abu-Safieh, A.S. Abu-Surrah, H.D. Tabba, H.A. AlMasri, R.M. Bawadi, F.M. Boudjelal, L.H. Tahtamouni, J. Chem. 2016 (2016).

[21] J. Haribabu, C. Balachandran, M.M. Tamizh, Y. Arun, N.S. Bhuvanesh, S. Aoki, R. Karvembu, J. Inorg. Biochem. (2020) 110988.

[22] X. Wei, Y. Yang, J. Ge, X. Lin, D. Liu, S. Wang, J. Zhang, G. Zhou, S. Li, J. Inorg. Biochem. 202 (2020) 110857.

[23] L. Fuentes, A.G. Quiroga, J.A. Organero, A.I. Matesanz, J. Inorg. Biochem. 203 (2020) 110875.

[24] M.N. Zafar, S. Masood, T.S.T. Muhammad, A.F. Dalebrook, M.F. Nazar, F.P. Malik, E.U. Mughal, L.J. Wright, Dalton Trans. 48 (2019) 15408-15418.

[25] T.T.H. Fong, C.N. Lok, C.Y.S. Chung, Y.M.E. Fung, P.K. Chow, P.K. Wan, C.M. Che, Angew. Chem. Int. Ed. 55 (2016) 11935-11939.

[26] J.D. Atwood Journal (1997) Pages.

[27] N.P. Barry, P.J. Sadler, Chem. Commun. 49 (2013) 5106-5131.

[28] B. Lippert Journal (1999) Pages.

[29] Y. Li, Z. Gu, C. Zhang, S. Li, L. Zhang, G. Zhou, S. Wang, J. Zhang, Eur. J. Med. Chem. 144 (2018) 662-671.

[30] M.M. Milutinović, A. Rilak, I. Bratsos, O. Klisurić, M. Vraneš, N. Gligorijević, S. Radulović, Ž.D. Bugarčić, J. Inorg. Biochem. 169 (2017) 1-12.

[31] P. Čanović, A.R. Simović, S. Radisavljević, I. Bratsos, N. Demitri, M. Mitrović, I. Zelen, Ž.D. Bugarčić, JBIC J. Biol. Inorg. Chem. 22 (2017) 1007-1028.

[32] D. Ćoćić, S. Jovanović, S. Radisavljević, J. Korzekwa, A. Scheurer, R. Puchta, D. Baskić, D. Todorović, S. Popović, S. Matić, J. Inorg. Biochem. 189 (2018) 91-102.

[33] R.O. Omondi, D. Jaganyi, S.O. Ojwach, A.A. Fatokun, Inorg. Chim. Acta. 482 (2018) 213-220.

[34] A.W. Addison, P.J. Burke, J. Heterocycl. Chem. 18 (1981) 803-805.

[35] P. Kopel, D. Wawrzak, V. Langer, K. Cihalova, D. Chudobova, R. Vesely, V. Adam, R. Kizek, Molecules, 20 (2015) 10360-10376.

[36] R.E. Rulke, J.M. Ernsting, A.L. Spek, C.J. Elsevier, P.W. van Leeuwen, K. Vrieze, Inorg. Chem. 32 (1993) 5769-5778.

[37] B. APeX, Bruker AXS Inc., Madison, Wisconsin, USA, 2010.

[38] G.M. Sheldrick, Acta Crystallographica Section C: Struct Chem, 71 (2015) 3-8.

[39] L.J. Farrugia, J. Appl. Crystallogr. 45 (2012) 849-854.

[40] M. Frisc, G. Trucks, H. Schlegel, G. Scuseria, M. Robb, J. Cheeseman, G. Scalmani, V. Barone, B. Mennucci, G. Petersson, Gaussian Inc, Wallingford, 2010.

[41] J. Li, L.-C. Xu, J.-C. Chen, K.-C. Zheng, L.-N. Ji, J. Phys. Chem. A. 110 (2006) 8174-8180.

[42] M. Cossi, G. Scalmani, N. Rega, V. Barone, J Chem Phys. 117 (2002) 43-54.

[43] R.G. Parr, L.v. Szentpály, S. Liu, J. Am. Chem. Soc. 121 (1999) 1922-1924.

[44] G. Macindoe, L. Mavridis, V. Venkatraman, M. Devignes, D. Ritchie, Medline, Google Scholar, 2010.

[45] H.R. Drew, R.M. Wing, T. Takano, C. Broka, S. Tanaka, K. Itakura, R.E. Dickerson, Proc. Natl. Acad. Sci. 78 (1981) 2179-2183.

[46] E. Pettersen, T. Goddard, C. Huang, G. Couch, D. Greenblatt, E. Meng, T. Ferrin, J. Comput. Chem. 25 (2004) 1605.

[47] C. Parker, W. Rees, Analyst, 87 (1962) 83-111.

[48] M. Puchalski, M. Morra, R. Von Wandruszka, Fresen J Anal Chem. 340 (1991) 341-344.

[49] S.O. Ojwach, I.A. Guzei, J. Darkwa, S.F. Mapolie, Polyhedron, 26 (2007) 851-861.

[50] W.M. Motswainyana, M.O. Onani, S.O. Ojwach, B. Omondi, Inorg. Chim. Acta. 391 (2012) 93-97.

[51] L. Yang, D.R. Powell, R.P. Houser, Dalton Trans. (2007) 955-964.

[52] I.J. Bruno, J.C. Cole, M. Kessler, J. Luo, W.S. Motherwell, L.H. Purkis, B.R. Smith, R. Taylor, R.I. Cooper, S.E. Harris, J Chem Inf Comput Sci. 44 (2004) 2133-2144.

[53] F.H. Allen, Crystallogr. B58 (2002) 380.

[54] M. Kosović, S. Jovanović, G.A. Bogdanović, G. Giester, Ž. Jaćimović, Ž.D. Bugarčić, B. Petrović, J Coord Chem. 69 (2016) 2819-2831.

[55] A. Mambanda, D. Jaganyi, Adv Inorg Chem. 70 (2017) 243-276.

[56] B. Petrović, Z.i.D. Bugarčić, A. Dees, I. Ivanović-Burmazović, F.W. Heinemann, R. Puchta, S.N. Steinmann, C. Corminboeuf, R. Van Eldik, Inorg. Chem. 51 (2012) 1516-1529.

[57] R. Van Eldik, T. Asano, W. Le Noble, Chem. Rev. 89 (1989) 549-688.

[58] M. Tobe, J. Burgess, Essex, 1999.

[59] R. Bellam, D. Jaganyi, A. Mambanda, R. Robinson, M.D. BalaKumaran, RSC Adv. 9 (2019) 31877-31894.

[60] R.K. Vuradi, K. Dandu, P.K. Yata, R.R. Mallepally, N. Chintakuntla, R. Ch, S.S. Thakur, C.M. Rao, S. Satyanarayana, New J. Chem. 42 (2018) 846-859.

[61] S. De, S.R. Chaudhuri, A. Panda, G.R. Jadhav, R.S. Kumar, P. Manohar, N. Ramesh, A. Mondal, A. Moorthy, S. Banerjee, New J. Chem. 43 (2019) 3291-3302.

[62] M. Howe-Grant, K.C. Wu, W.R. Bauer, S.J. Lippard, Biochemistry, 15 (1976) 4339-4346.

[63] G.K. Mutua, R. Bellam, D. Jaganyi, A. Mambanda, J Coord Chem.72 (2019) 2931-2956.

[64] E. Sindhuja, R. Ramesh, N. Dharmaraj, Y. Liu, Inorg. Chim. Acta. 416 (2014) 1-12.

[65] S. Mondal, M. Chakraborty, A. Mondal, B. Pakhira, A.J. Blake, E. Sinn, S.K. Chattopadhyay, New J. Chem. 42 (2018) 9588-9597.

[66] I. Mitra, S. Mukherjee, B. Misini, P. Das, S. Dasgupta, W. Linert, S.C. Moi, New J. Chem. 42 (2018) 2574-2589.

[67] R.R. Monaco, J. Biomol. Struct. Dyn. 25 (2007) 119-125.

[68] Z. Liu, A. Habtemariam, A.M. Pizarro, S.A. Fletcher, A. Kisova, O. Vrana, L. Salassa, P.C. Bruijnincx, G.J. Clarkson, V. Brabec, J. Med. Chem. 54 (2011) 3011-3026.

[69] M. Tian, J. Li, S. Zhang, L. Guo, X. He, D. Kong, H. Zhang, Z. Liu, Chem. Commun. 53 (2017) 12810-12813.

[70] S. Mukherjee, I. Mitra, P. Das, B. Misini, W. Linert, S.C. Moi, ChemistrySelect, 3 (2018) 3871-3885.

[71] A.A. Fatokun, T.W. Stone, R.A. Smith, Front. Biosci. 13 (2008) 3288-3311.

[72] W. Yu, Y. Chen, J. Dubrulle, F. Stossi, V. Putluri, A. Sreekumar, N. Putluri, D. Baluya, S.Y. Lai, V.C. Sandulache, Sci. Rep. 8 (2018) 1-12.

[73] A. Tkachenko, A. Onishchenko, V. Gopkalov, T. Gorbach, E. Kharchenko, D. Sklyaruk. Med. Rev 4 (2019) 32–37

[74] A.A. Fatokun, V.L. Dawson, T.M. Dawson, Br. J. Pharmacol. 171 (2014) 2000-2016.

[75] L. Galluzzi, I. Vitale, S.A. Aaronson, J.M. Abrams, D. Adam, P. Agostinis, E.S. Alnemri, L. Altucci, I. Amelio, D.W. Andrews, Cell Death Differ. 25 (2018) 486-541.

[76] Y. Xu, C. Wang, Z. Li, Mol Clin Oncol. 2 (2014) 3-7.

SUPPORTING INFORMATION

Palladium(II) complexes of tridentate bis(benzoazole) ligands: structural, substitution kinetics, DNA interactions and cytotoxicity studies

Reinner O. Omondi[a], Rajesh Bellam[a], Stephen O. Ojwach[a], Deogratius Jaganyi[b, c], Amos A. Fatokun[d]

[a] School of Chemistry and Physics, University of KwaZulu-Natal, Private Bag X01, Scottsville, Pietermaritzburg 3209, South Africa.

[b] School of Science, College of Science and Technology, University of Rwanda, P.O. Box 4285, Kigali, Rwanda.

[c] Department of Chemistry, Faculty of Applied Sciences, Durban University of Technology, P.O. Box 1334, Durban 4000, South Africa

[d] Centre for Natural Products Discovery (CNPD), School of Pharmacy and Biomolecular Sciences, Faculty of Science, Liverpool John Moores University, Liverpool L3 3AF, UK.

Supporting information
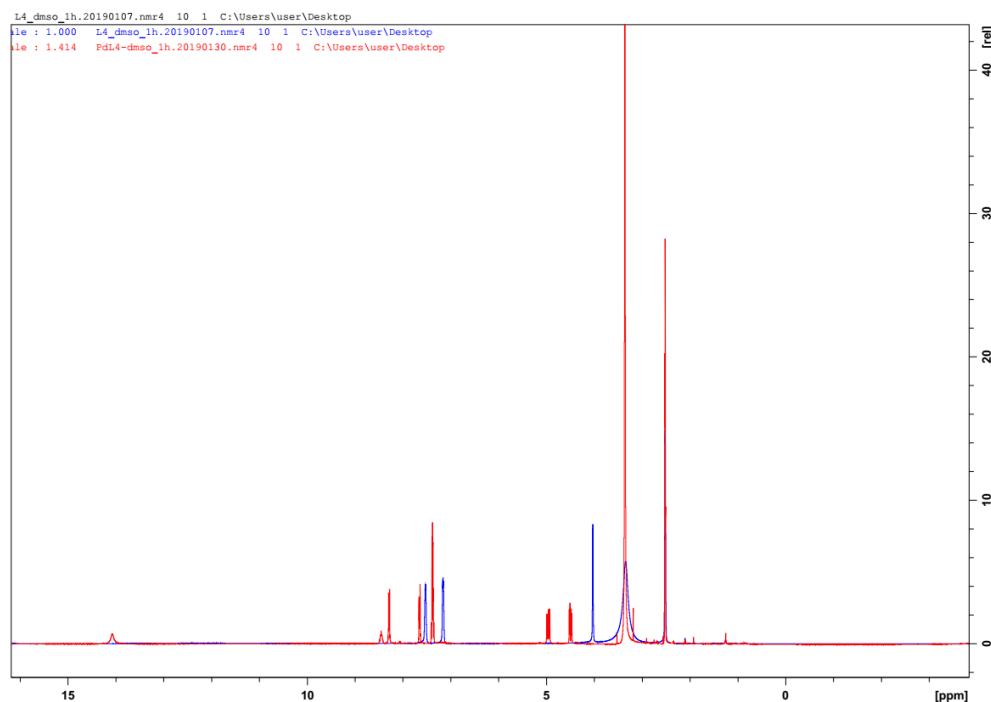
Figure S1: ^{1}H NMR overlay for ligand **L₄** and **PdL₄**
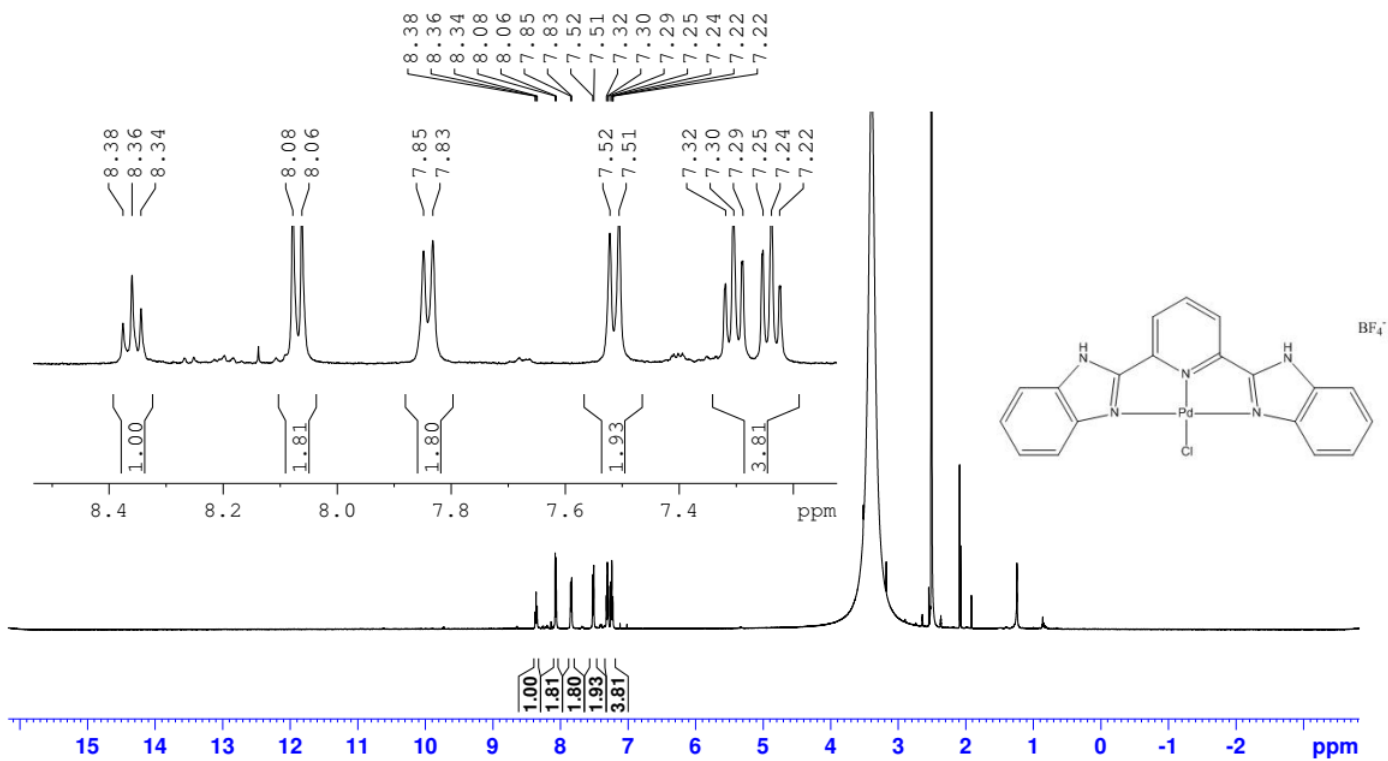
Figure S2: ^{1}H NMR spectrum of **PdL$_1$**
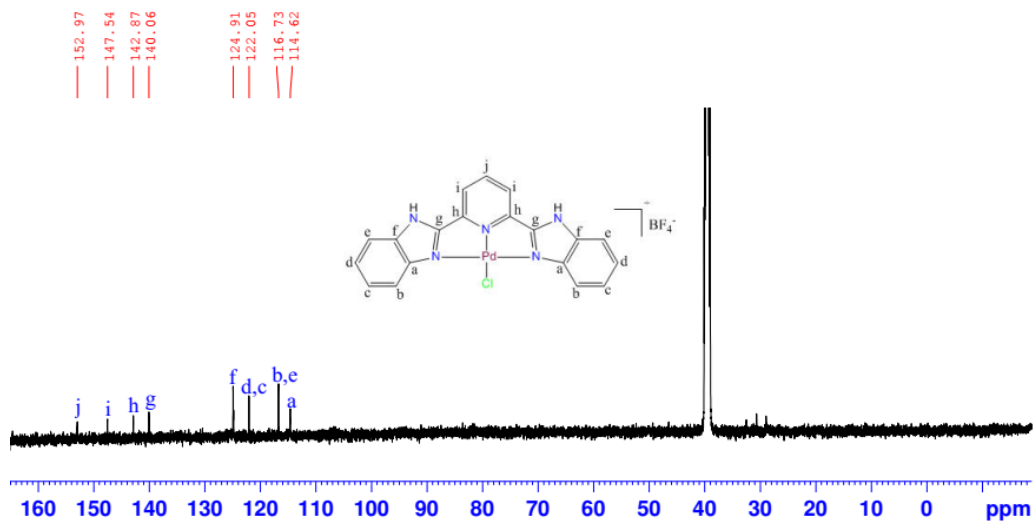
Figure S3: ^{13}C NMR spectrum of **PdL$_1$**
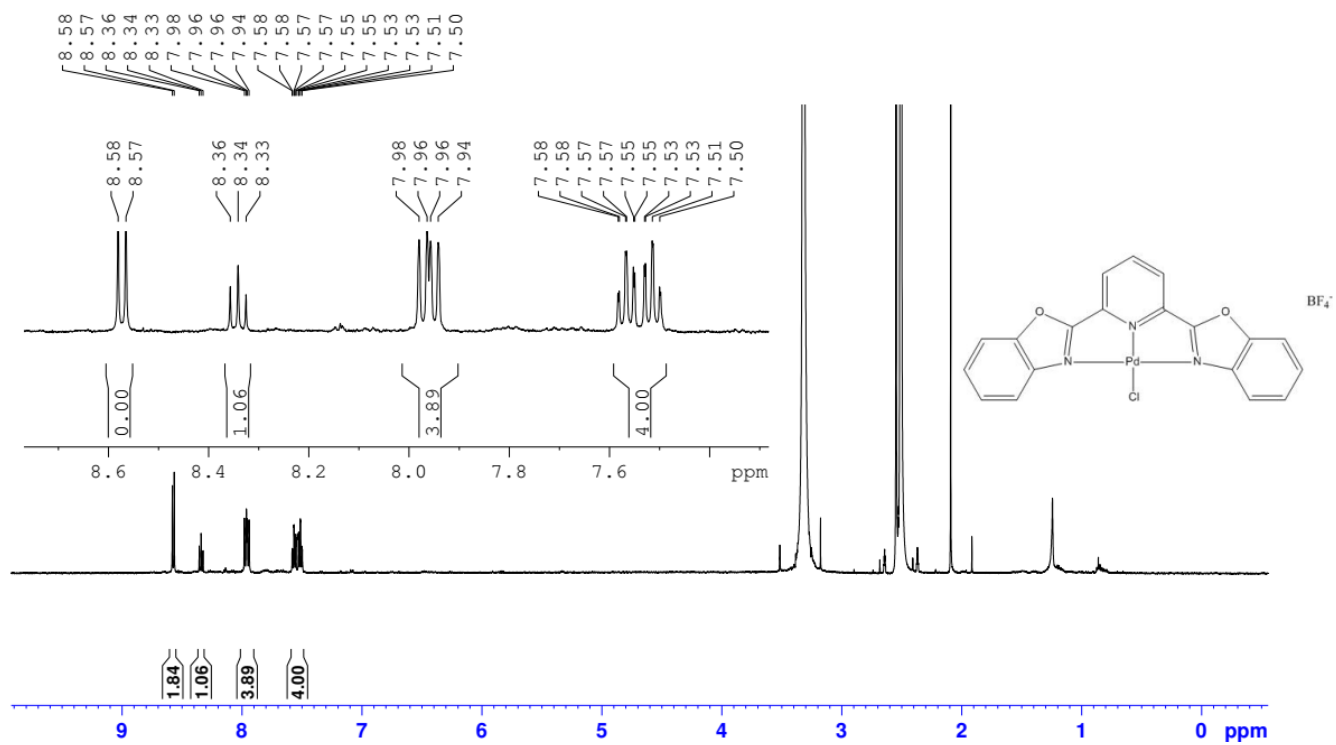
Figure S4: ^{1}H NMR spectrum of **PdL₂**
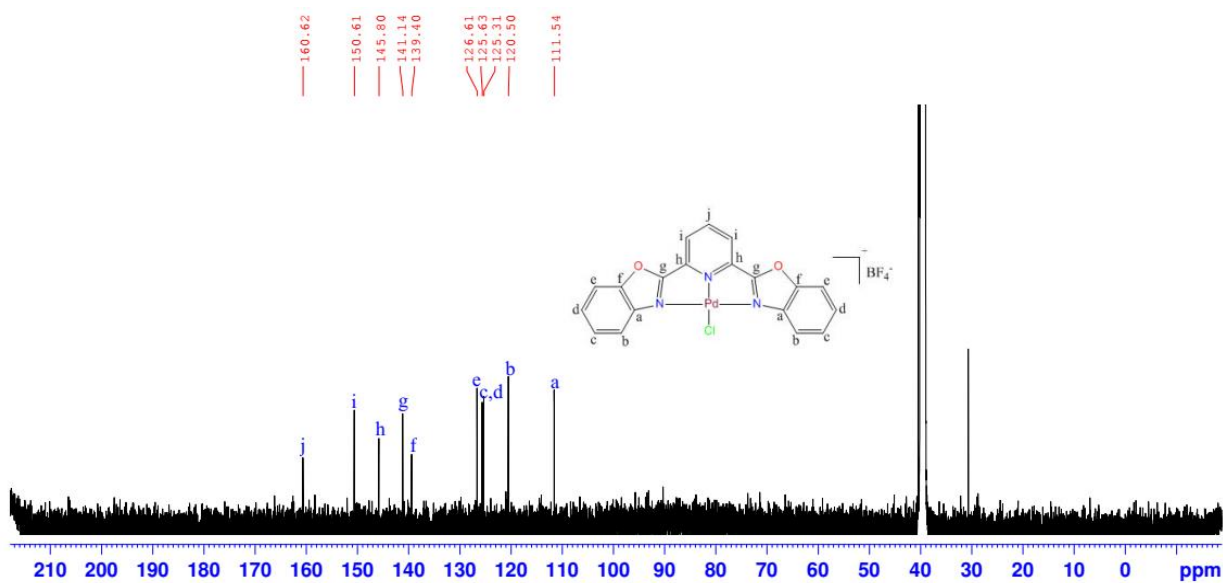
Figure S5: ^{13}C NMR spectrum of **PdL₂**
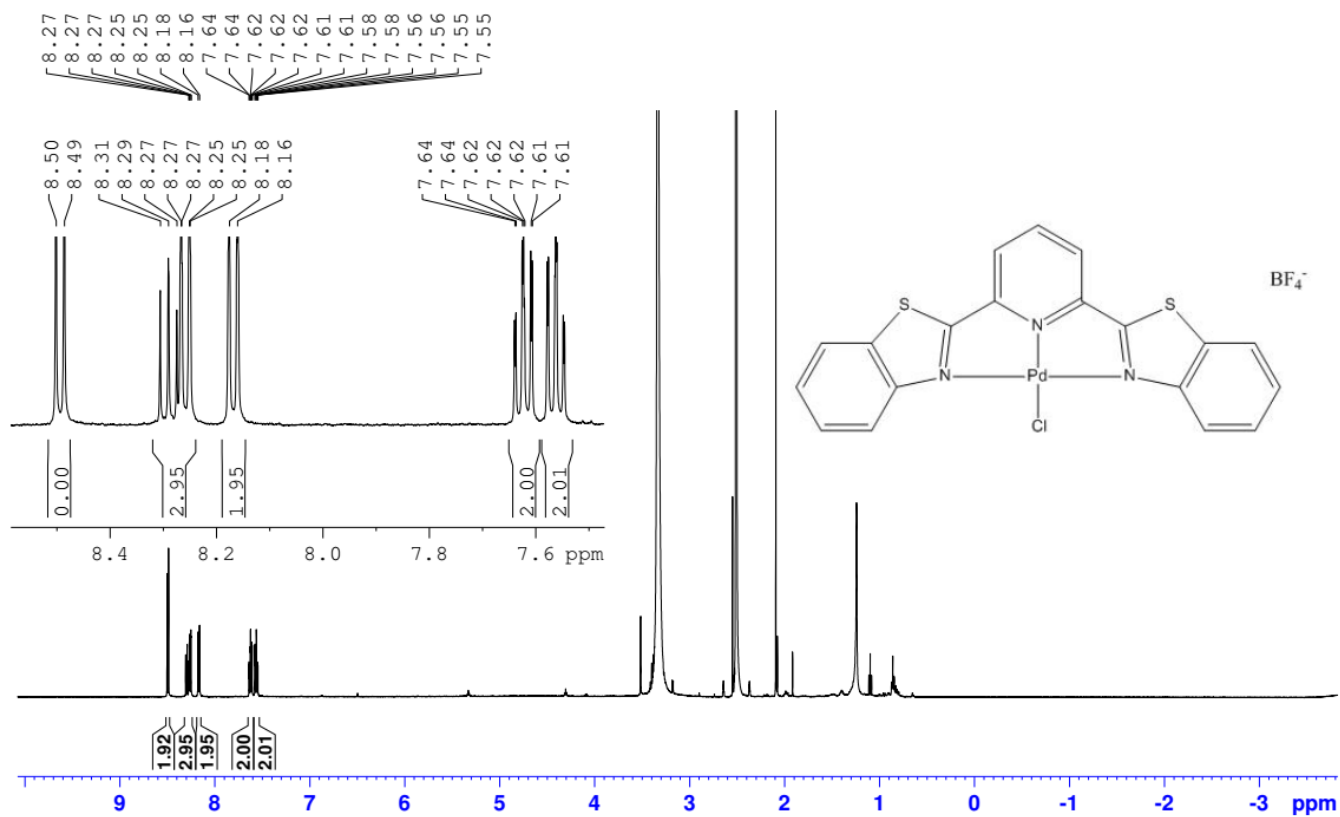
Figure S6: ^{1}H NMR spectrum of **PdL$_3$**
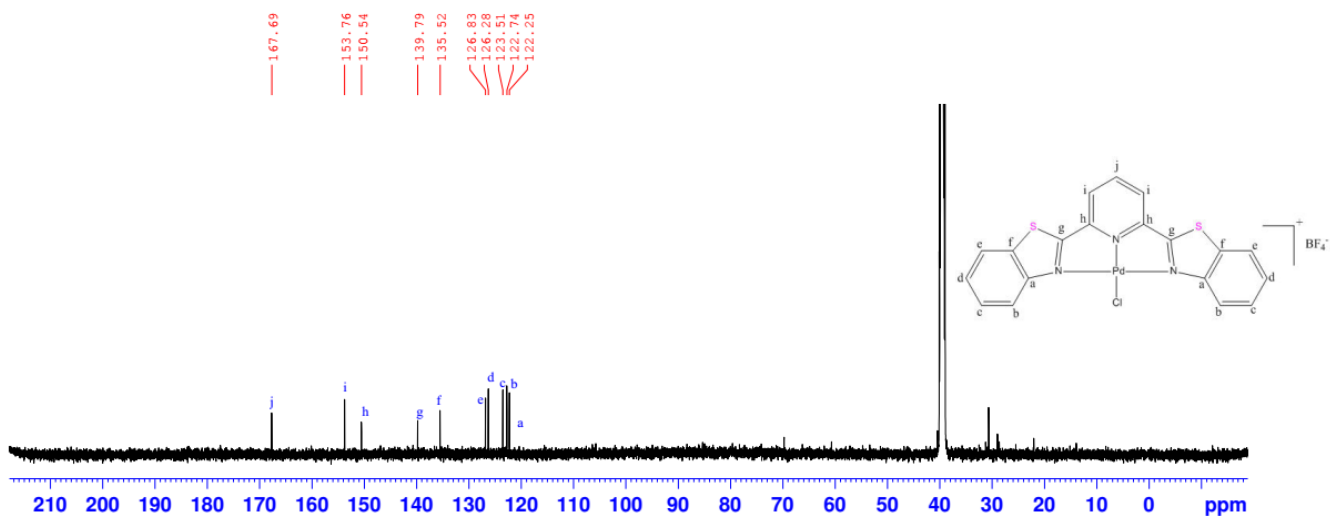
Figure S7: ^{13}C NMR spectrum of **PdL3**
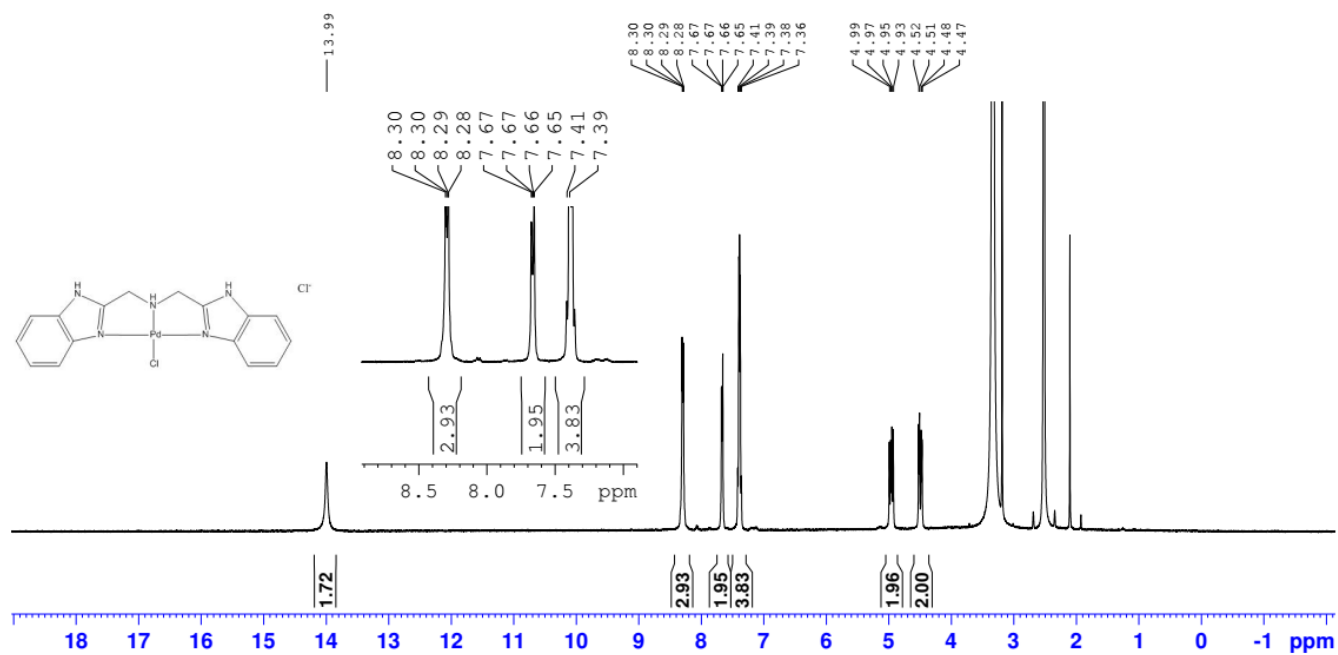
Figure S8: ^{1}H NMR spectrum of **PdL$_4$**
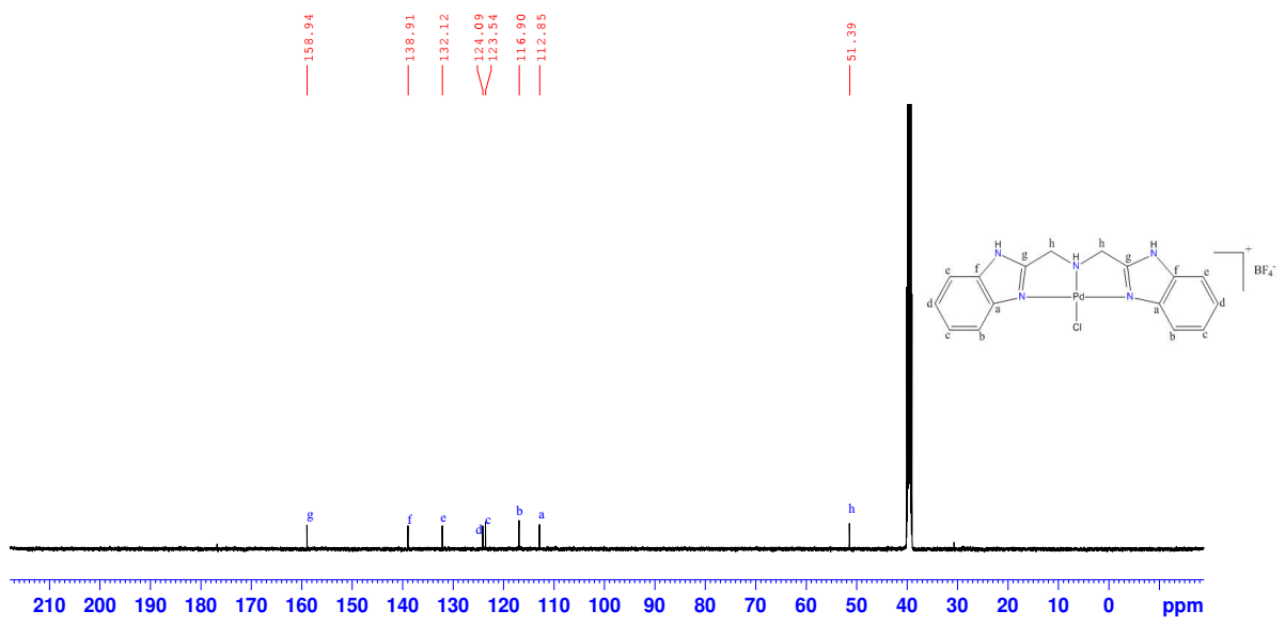
Figure S9: ^{13}C NMR spectrum of **PdL$_4$**
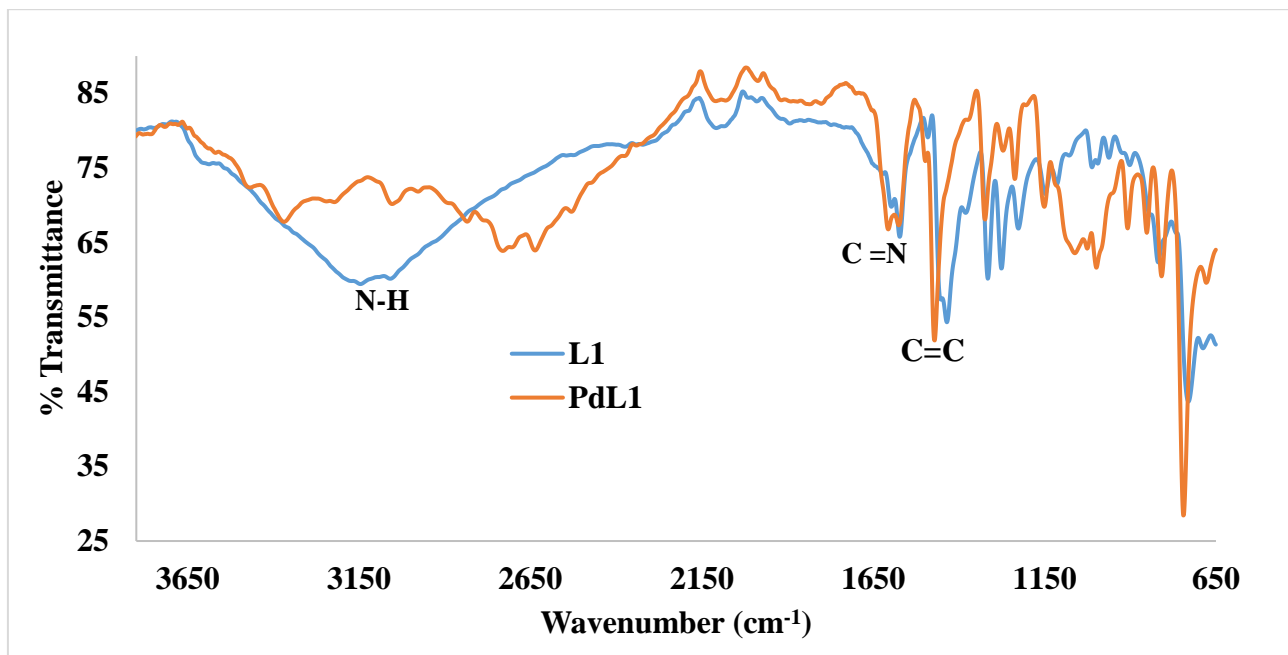
Figure S10: FTIR overlay for **L$_1$** and **PdL$_1$**
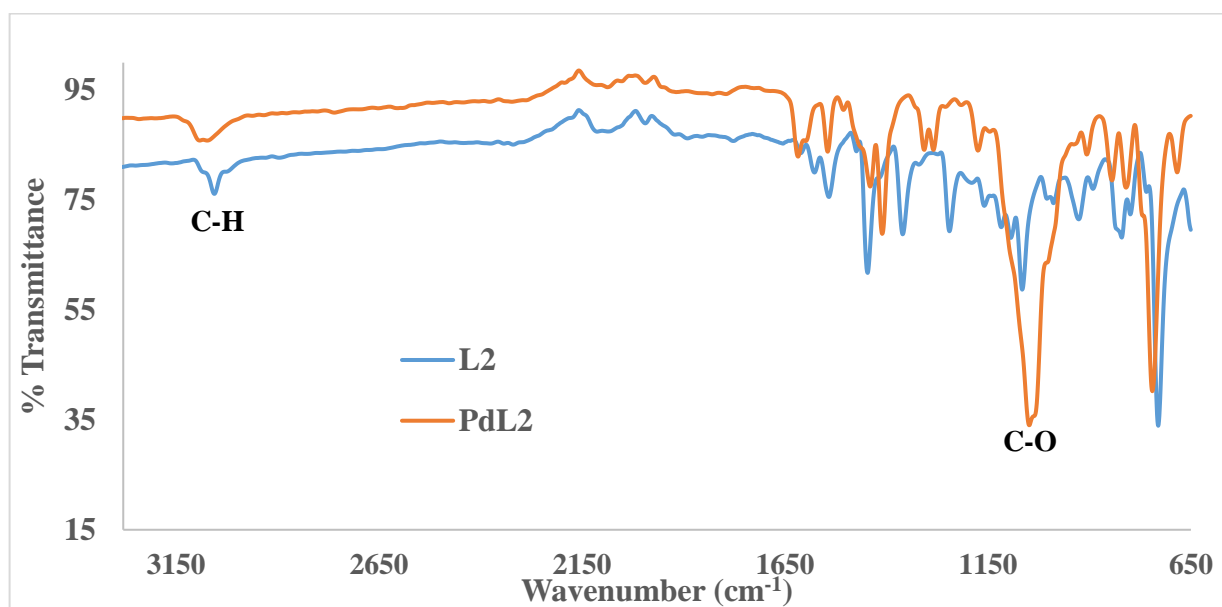
S11: FTIR overlay for **L$_2$** and **PdL$_2$**
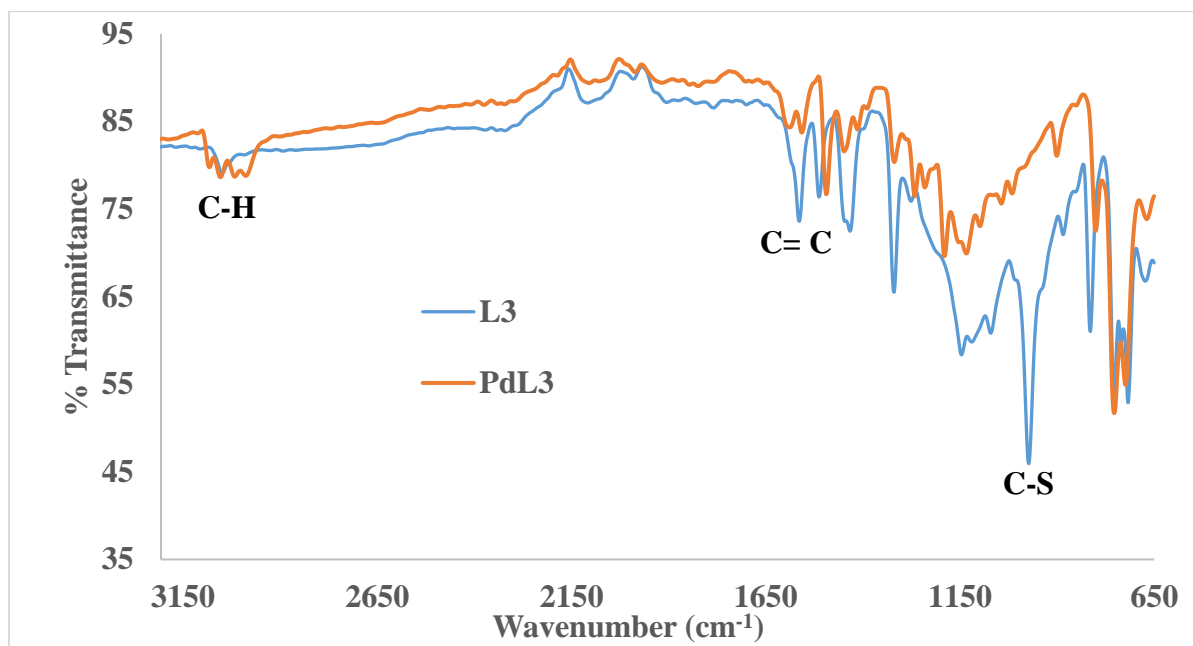
Figure

Figure S12: FTIR overlay for **L₃** and **PdL₃**
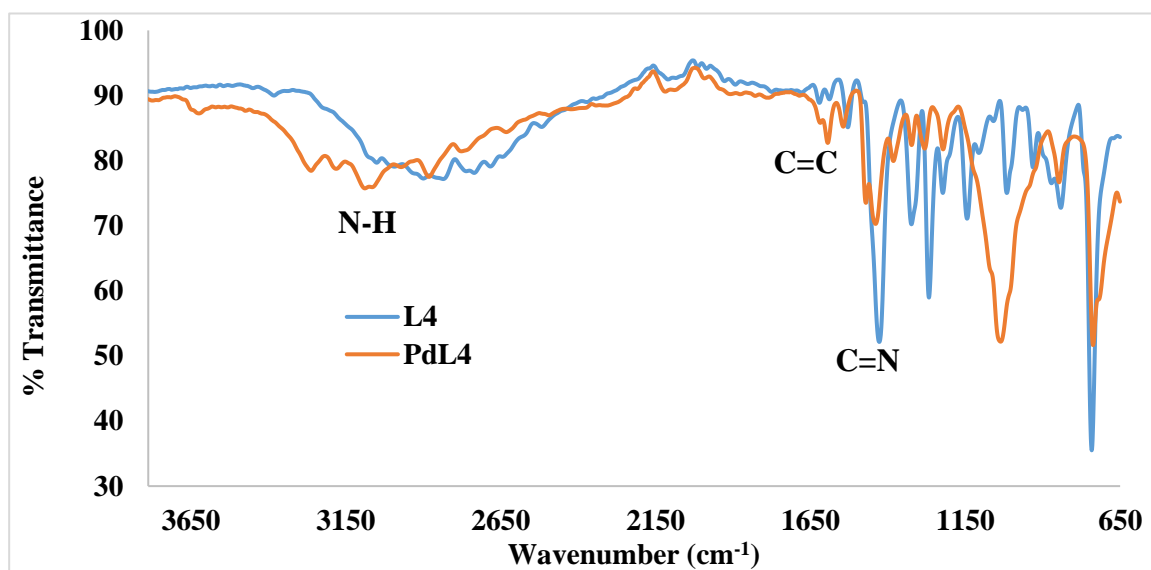
Figure S13: FTIR overlay for **L₄** and **PdL₄**
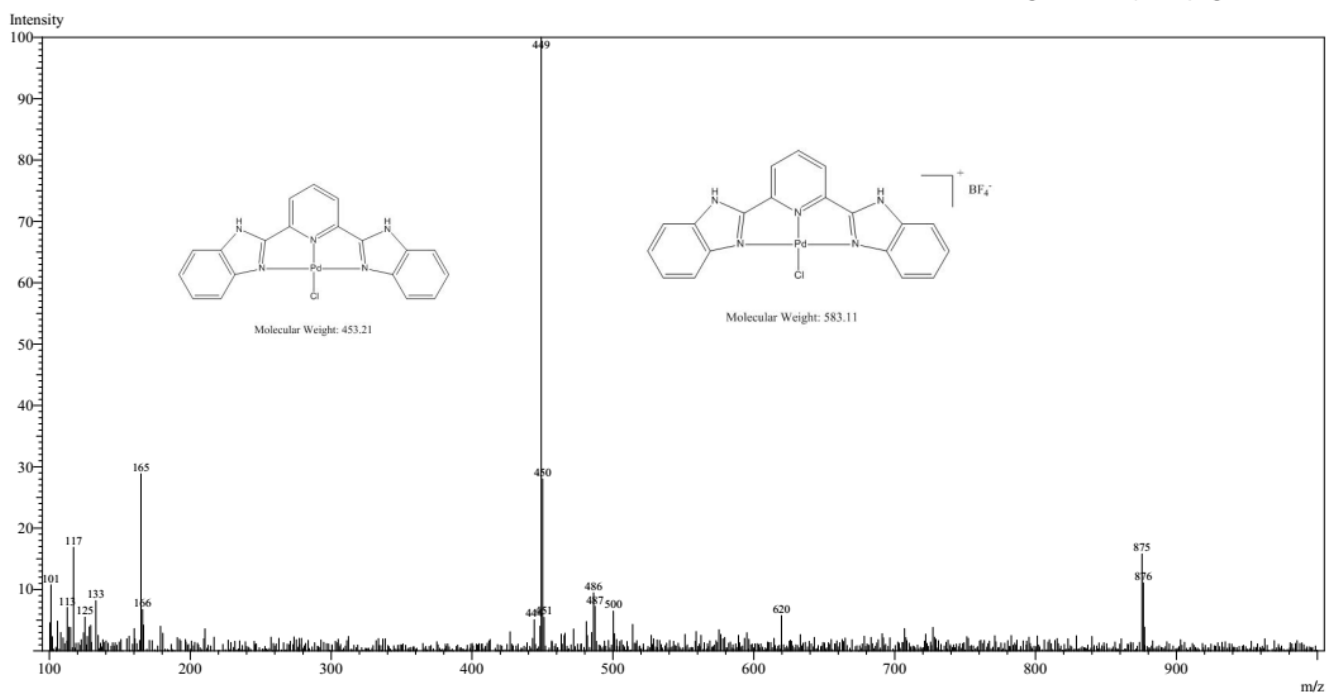
Figure S14: Mass spectrum of **PdL₁** showing the *m/z* = 451 corresponding to its molar mass
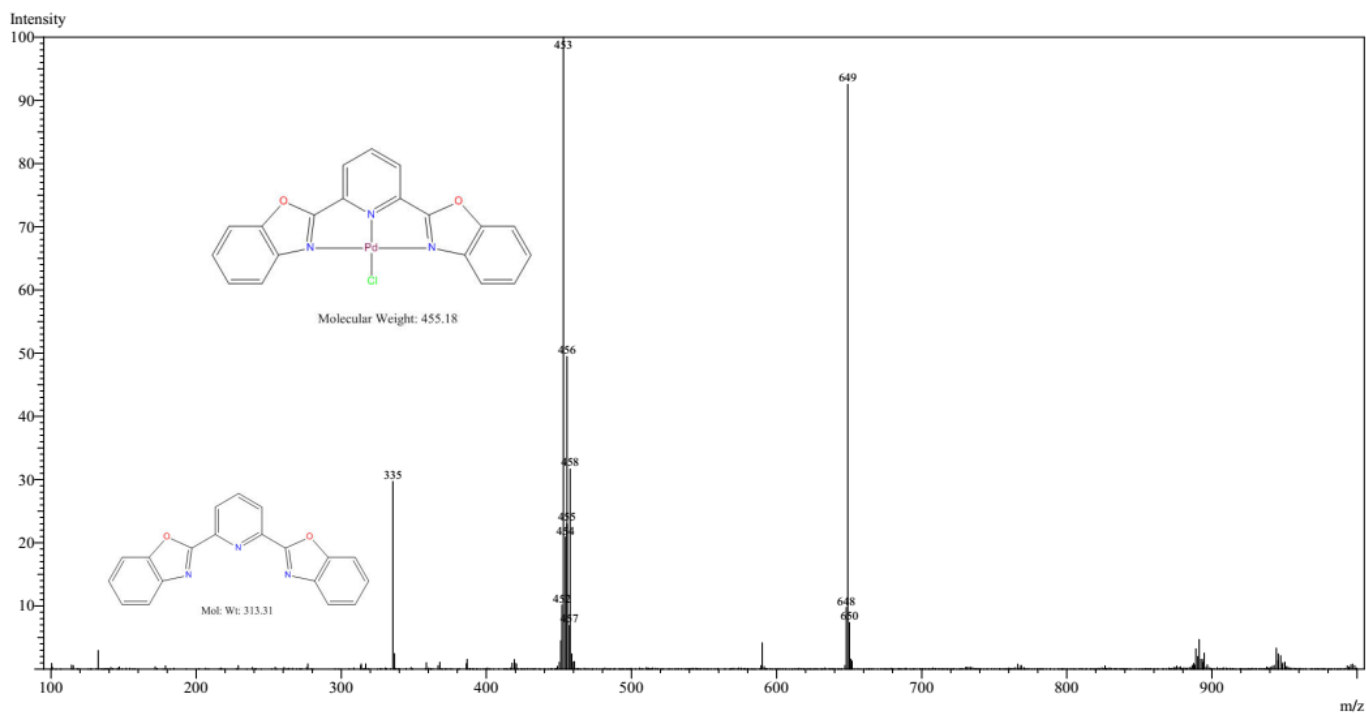
Figure S15: Mass spectrum of **PdL₂** showing the *m/z* = 453 corresponding to its molar mass
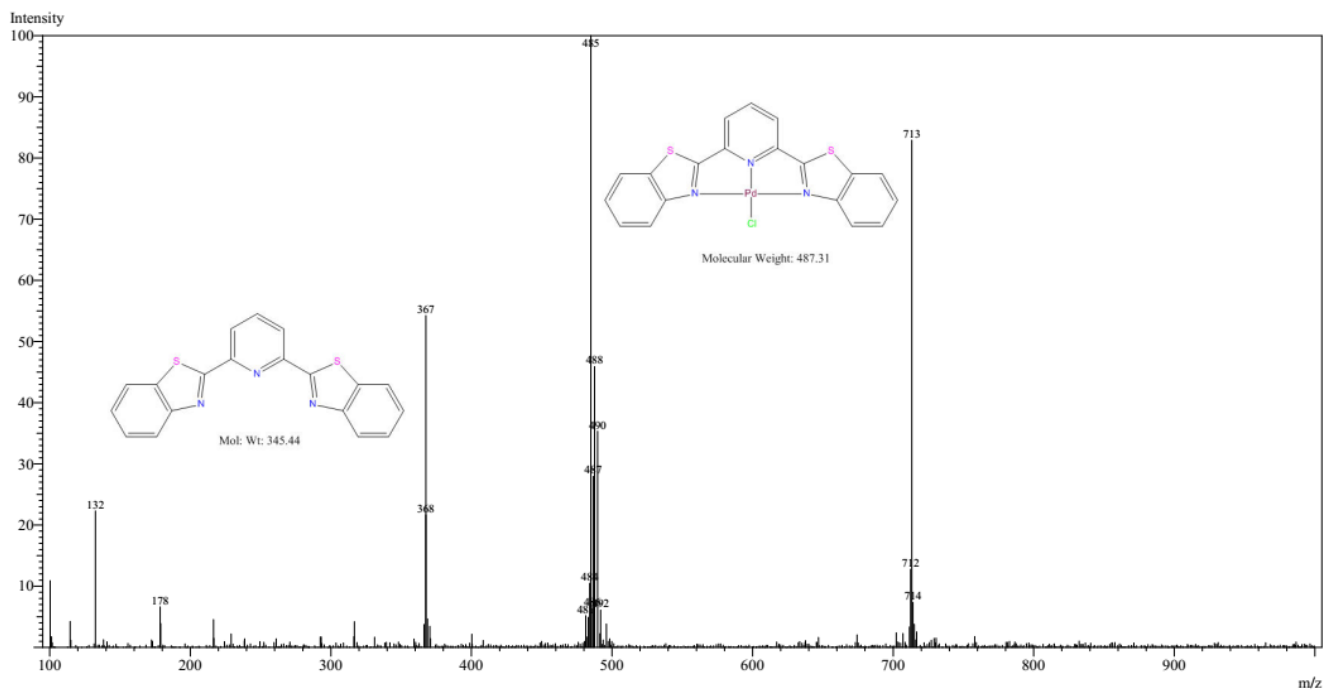
Figure S16: Mass spectrum of **PdL₃** showing the *m/z* = 485 corresponding to its molar mass
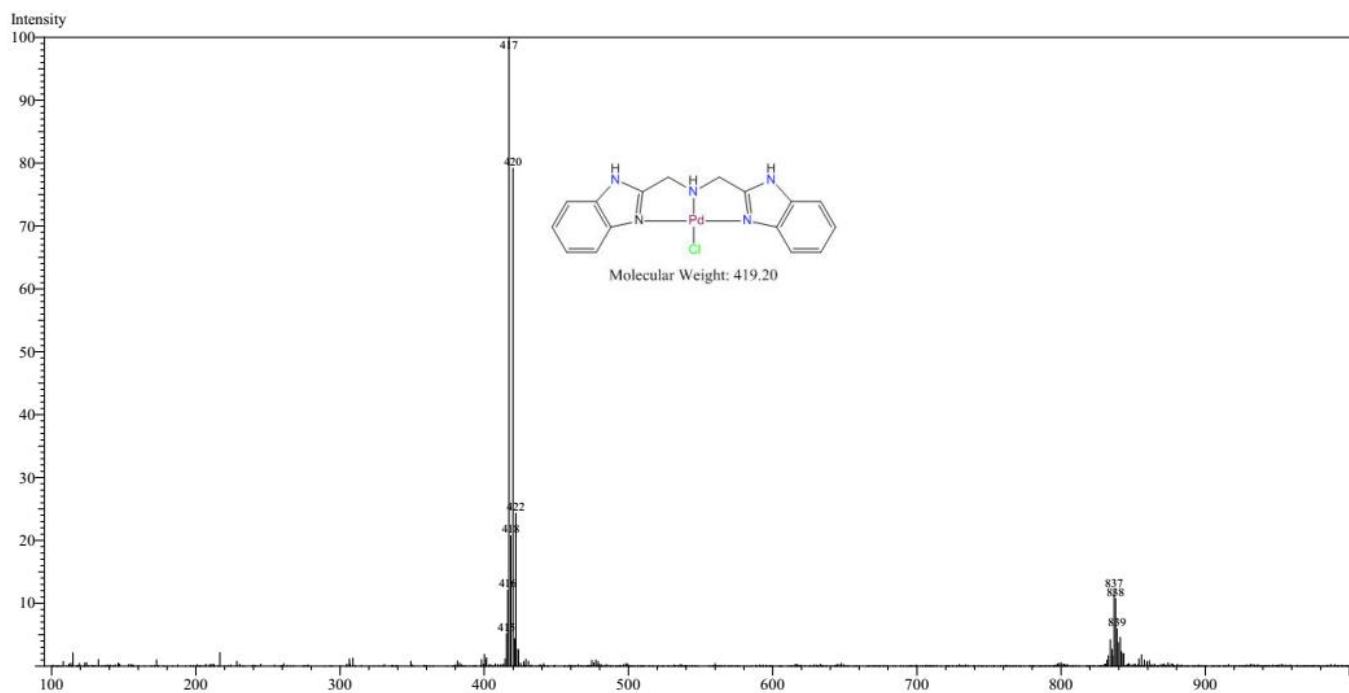
Figure S17: Mass spectrum of **PdL₄** showing the *m/z* = 417 corresponding to its molar mass
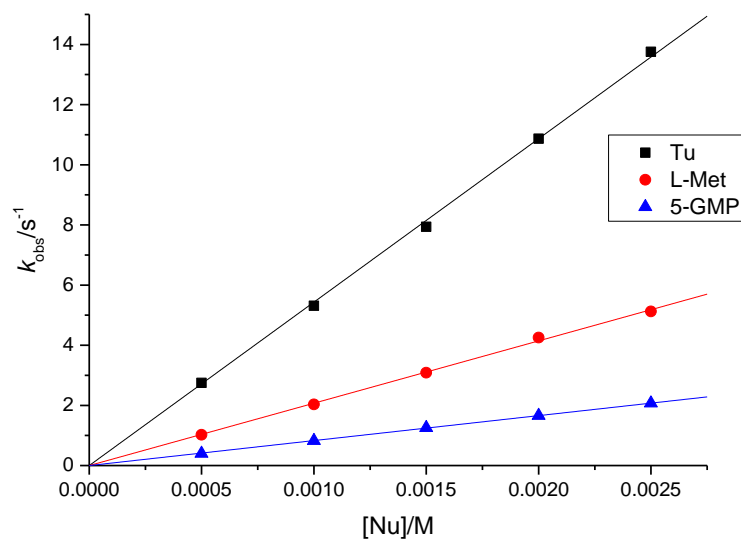
Figure S18: Dependence of k_{obs} on the nucleophile concentration for chloride substitution from **PdL₂** at T = 298 K, 25mM Hepes buffer (pH =7.2) and 10 mM NaCl.
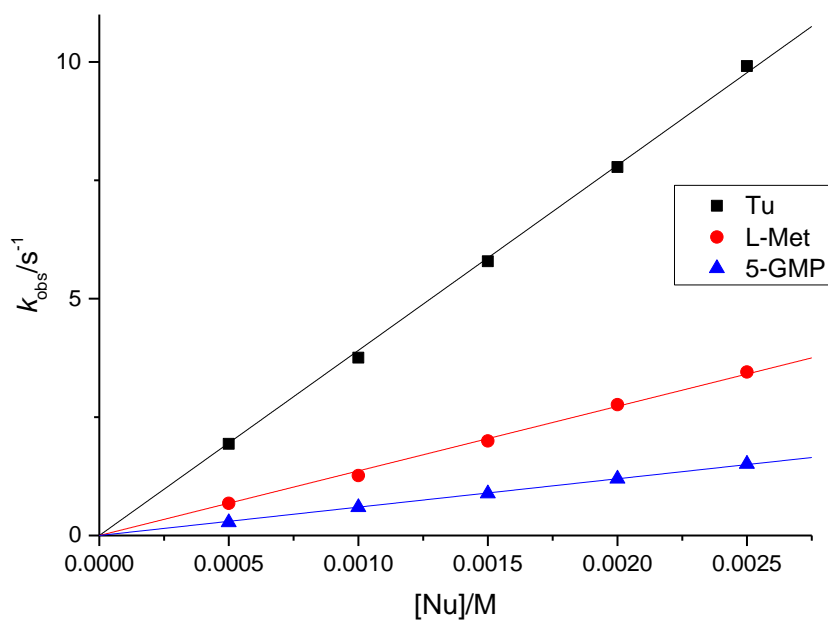
Figure S19: Dependence of k_{obs} on the nucleophile concentration for chloride substitution from **PdL₃** at T = 298 K, 25mM Hepes buffer (pH =7.2) and 10 mM NaCl.
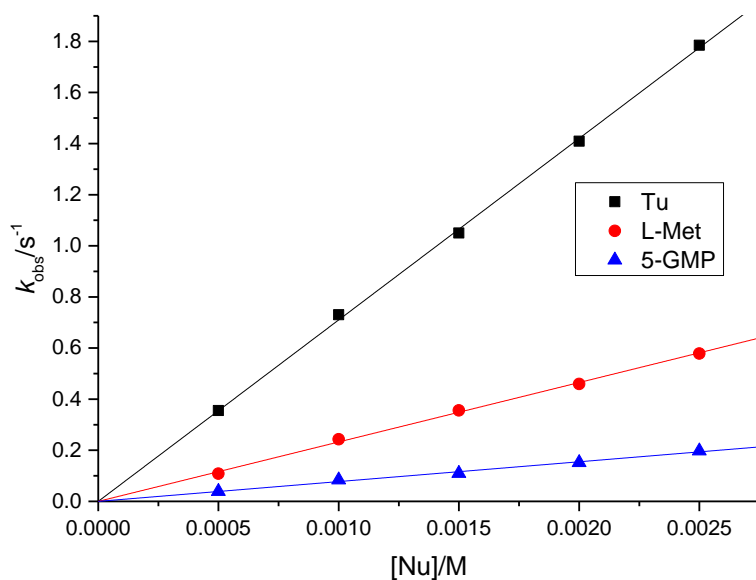
Figure S20: Dependence of k_{obs} on the nucleophile concentration for chloride substitution from **PdL$_4$** at T = 298 K, 25mM Hepes buffer (pH =7.2) and 10 mM NaCl.
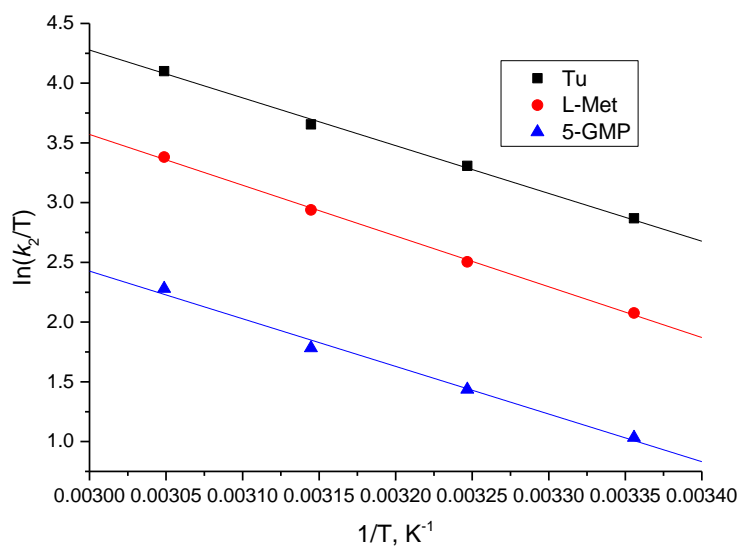
Figure S21: Eyring plots for the reaction of **PdL$_2$** with nucleophiles in aqua, 25 mM Hepes buffer (pH =7.2) and 10 mM NaCl.
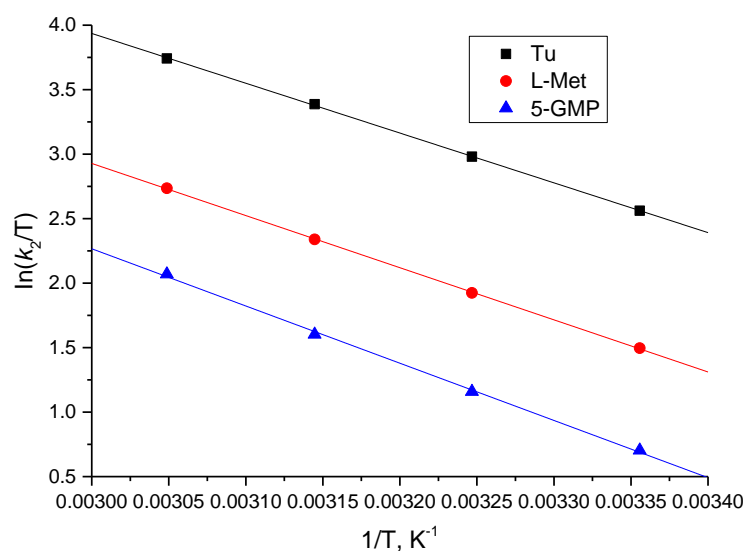
Figure S22: Eyring plots for the reaction of **PdL₃** with the nucleophiles in aqua, 25 mM Hepes buffer (pH =7.2) and 10 mM NaCl.

Equation	y = a + b*x		
Weight	No Weighting		
Residual Sum of	3.25583E-4	6.07496E-6	1.78697E-4
Pearson's r	-0.99971	-0.99999	-0.99978
Adj. R-Squar	0.99914	0.99998	0.99933
		Value	Standard Erro
Tu	Intercept	10.05406	0.17549
	Slope	-3240.7130	54.80446
L-Met	Intercept	7.69241	0.02397
	Slope	-2777.5027	7.48613
5-GMP	Intercept	6.76394	0.13001
	Slope	-2712.2356	40.60173
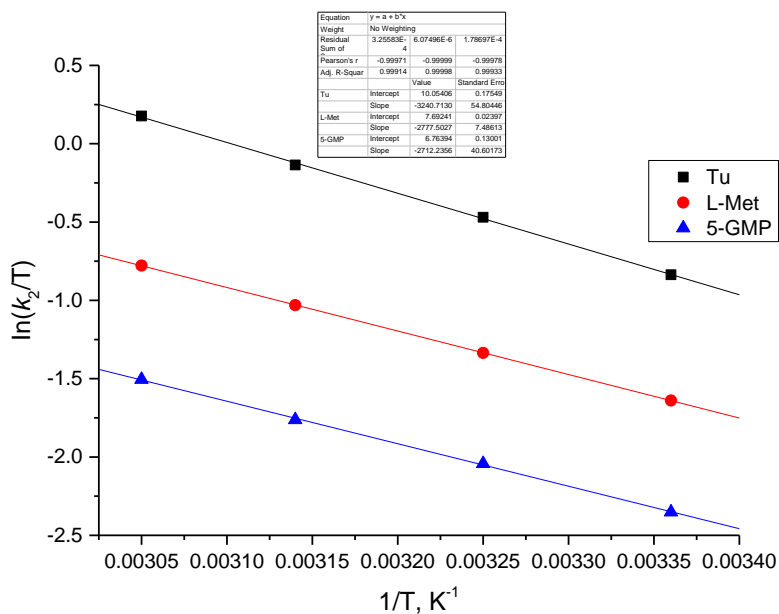
Figure S23: Eyring plots for the reaction of **PdL₃** with the nucleophiles in aqua, 25 mM Hepes buffer (pH =7.2) and 10 mM NaCl.
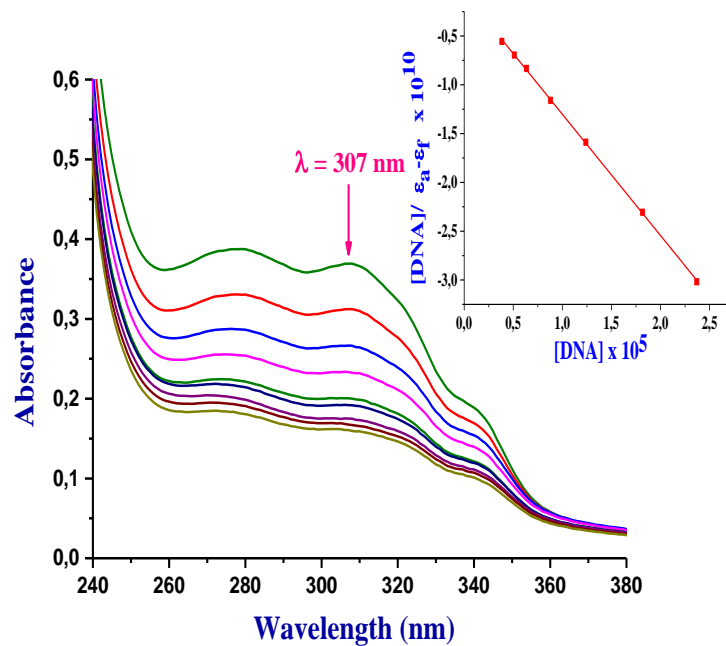
Figure S24: Absorption spectra of **PdL₂** complex (20 μM) in Tris-HCl/50 mM buffer at pH 7.2 upon addition of CT-DNA (0 - 40 μM). The arrow shows the change in absorbance upon increasing the CT-DNA concentration. Inset: plot of [CT-DNA] versus [DNA]/(ε_a- ε_f).
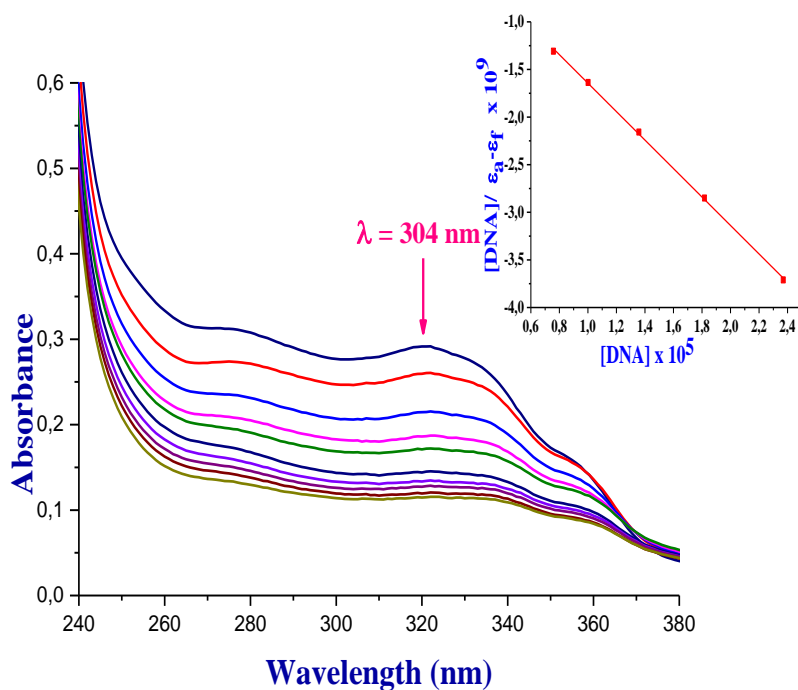
Figure S25: Absorption spectra of **PdL₃** complex (20 μM) in Tris-HCl/50 mM buffer at pH 7.2 upon addition of CT-DNA (0 - 40 μM). The arrow shows the change in absorbance upon increasing the CT-DNA concentration. Inset: plot of [CT-DNA] versus $[DNA]/(\varepsilon_a - \varepsilon_f)$.
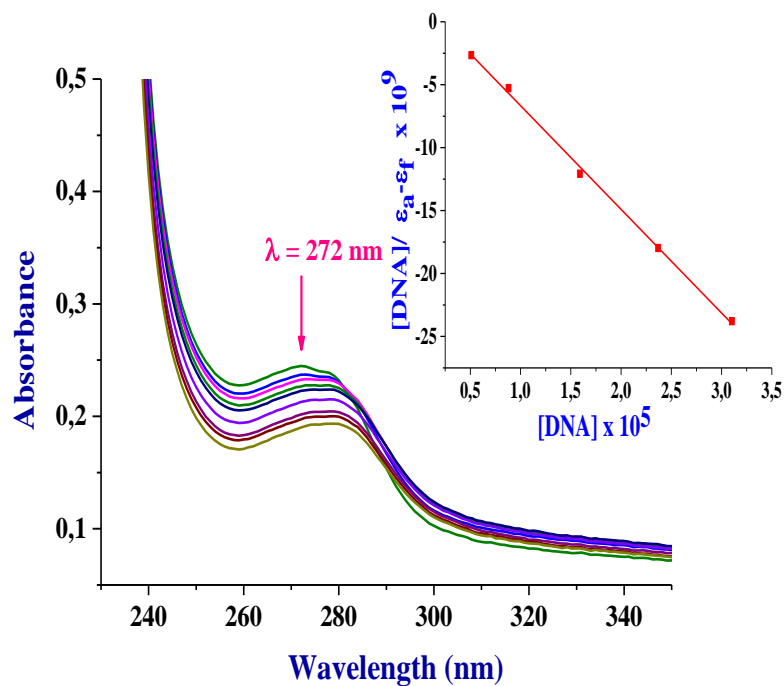
Figure S26: Absorption spectra of **PdL₄** complex (20 μM) in Tris-HCl/50 mM buffer at pH 7.2 upon addition of CT-DNA (0 - 40 μM). The arrow shows the change in absorbance upon increasing the CT-DNA concentration. Inset: plot of [CT-DNA] versus $[DNA]/(\varepsilon_a - \varepsilon_f)$.
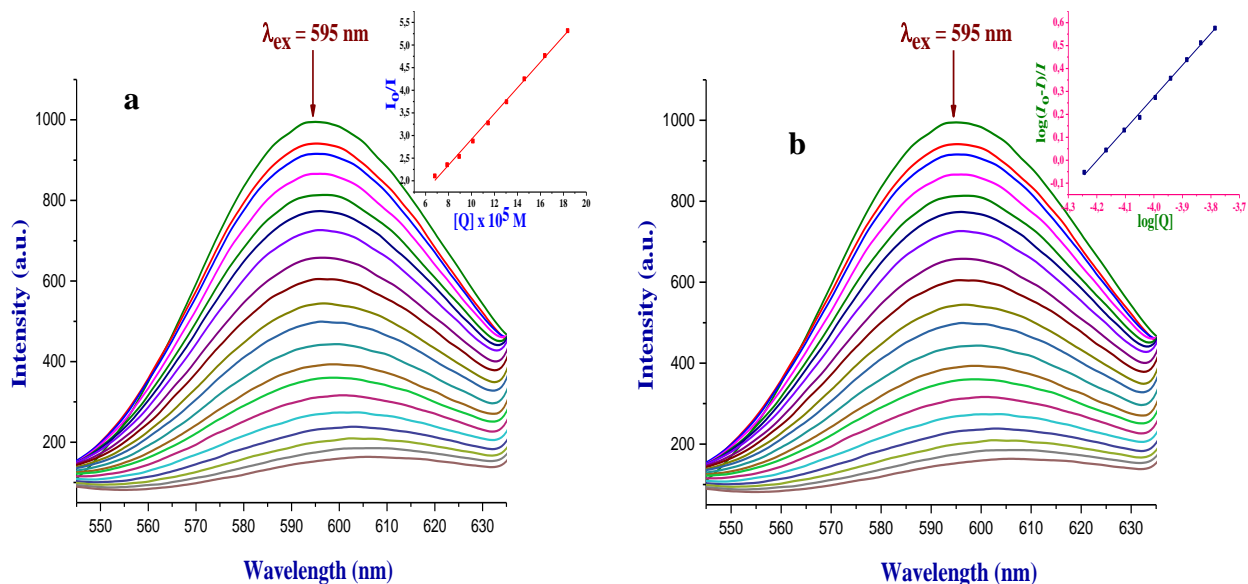
Figure S27: Fluorescence emission spectra of EB bounded to CT-DNA in the presence of **PdL₂**: [EB] = 6.5 μM, [CTDNA] = 6.5 μM and [**PdL₂**] = 0-200 μM. The arrow shows the intensity changes upon increasing the **PdL₂** complex concentration; **(a)** Stern-Volmer plot of I_o/I versus [Q]; **(b)** Scatchard plot of $\log[(I_o-I)/I]$ versus $\log[Q]$.
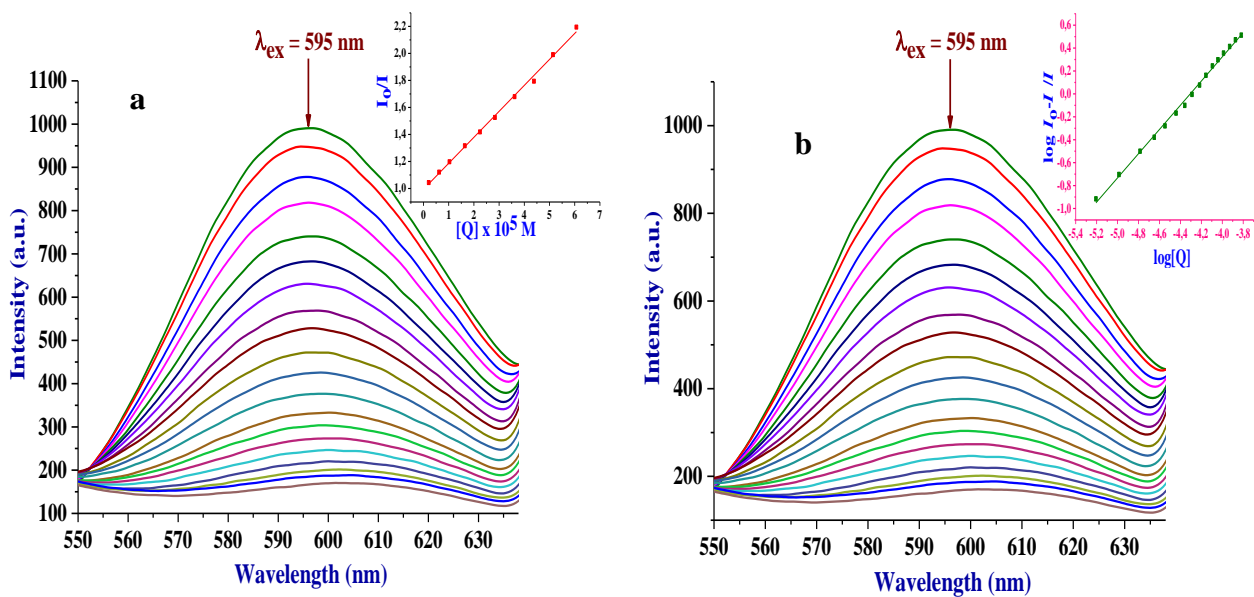
Figure S28: Fluorescence emission spectra of EB bounded to CT-DNA in the presence of **PdL₃**: [EB] = 6.5 μM, [CTDNA] = 6.5 μM and [**PdL₃**] = 0-200 μM. The arrow shows the intensity changes upon increasing the **PdL₃** complex concentration; **(a)** Stern-Volmer plot of I_o/I versus [Q]; **(b)** Scatchard plot of $\log[(I_o–I)/I]$ versus $\log[Q]$.
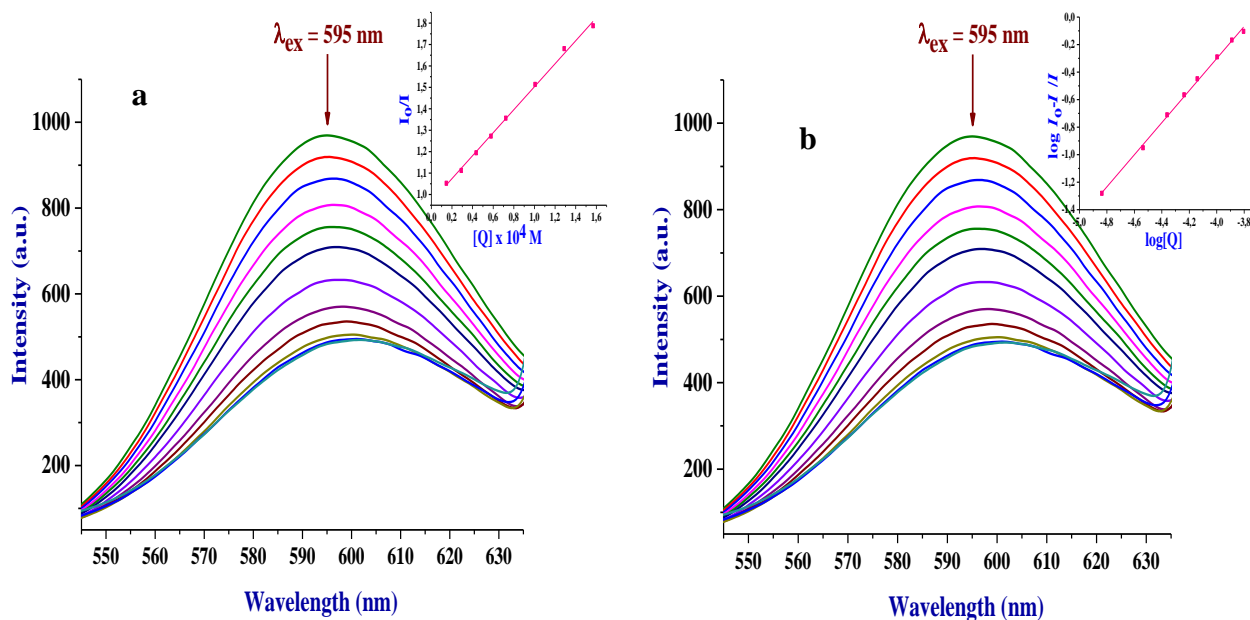
Figure S29: Fluorescence emission spectra of EB bounded to CT-DNA in the presence of **PdL₄**: [EB] = 6.5 μM, [CTDNA] = 6.5 μM and [**PdL₄**] = 0-200 μM. The arrow shows the intensity changes upon increasing the **PdL₄** complex concentration; **(a)** Stern-Volmer plot of I_o/I versus [Q]; **(b)** Scatchard plot of $\log[(I_o–I)/I]$ versus $\log[Q]$.
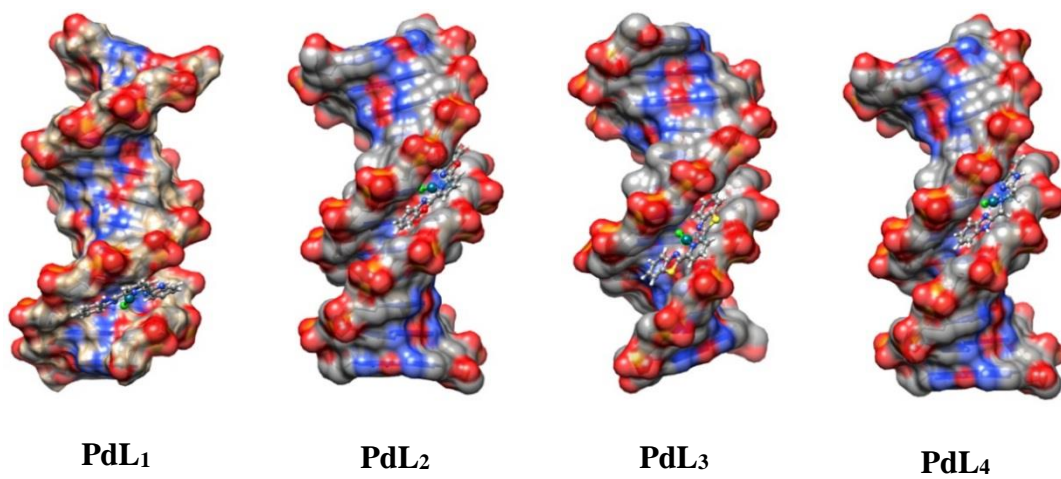
PdL₁   **PdL₂**   **PdL₃**   **PdL₄**

Figure S30: Computational docking models illustrating the interactions of **PdL₁**, **PdL₂**, **PdL₃**, and **PdL₄** with B-DNA duplex, with docking score of -270.07, -268.81, -266.11, and -263.96 Kcal/Mol, respectively.
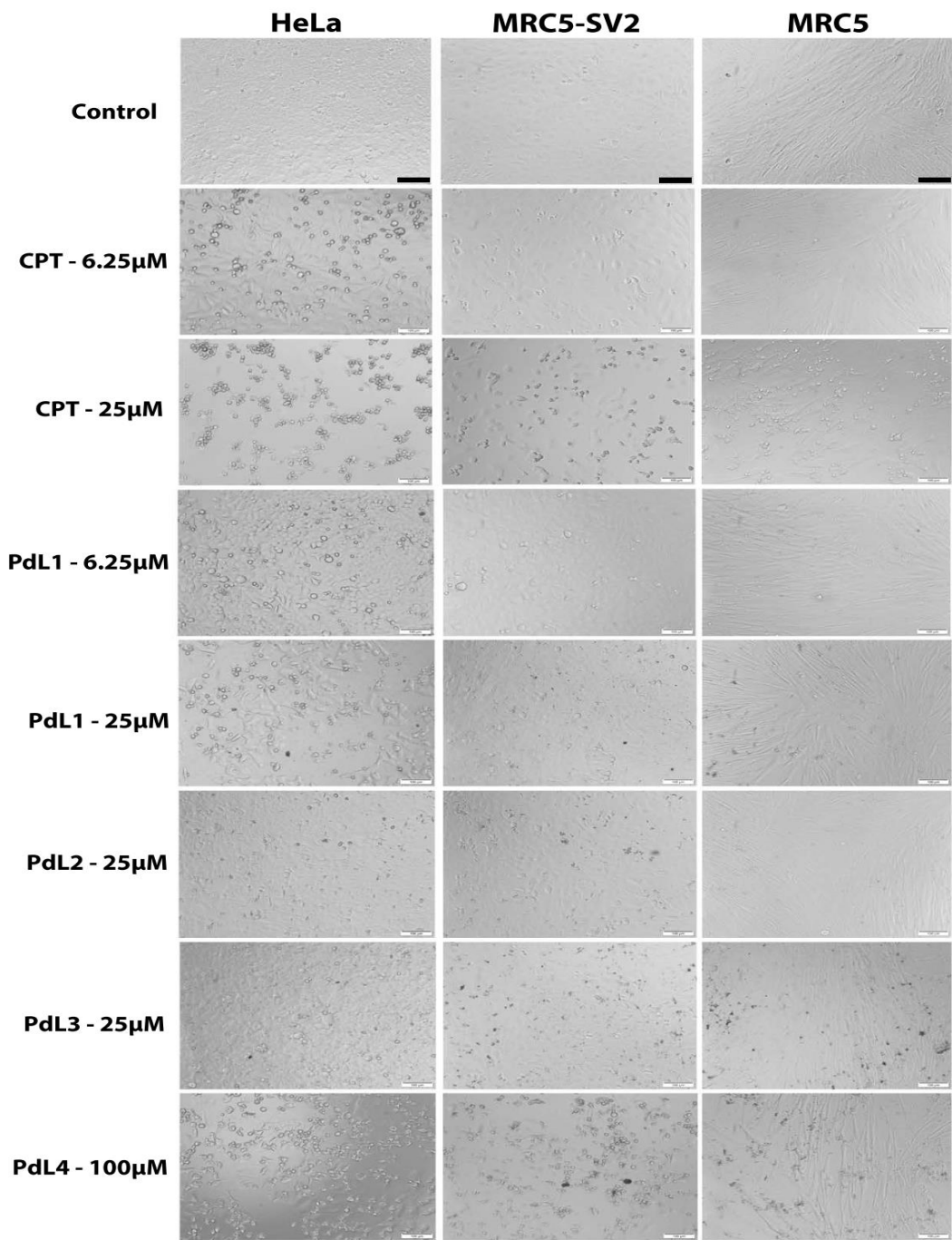
Figure S31: Morphological damage for each of the cell lines
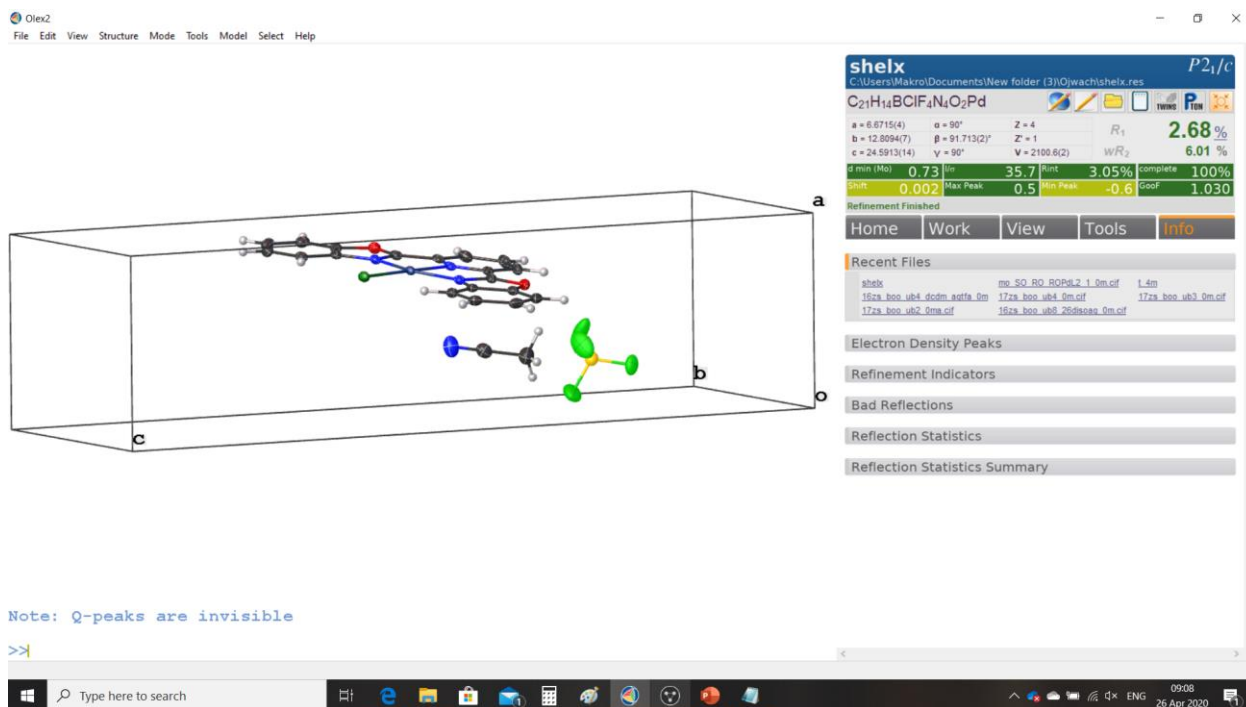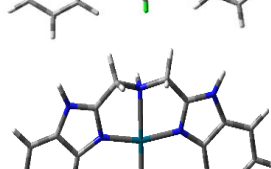
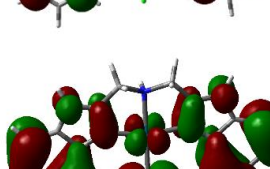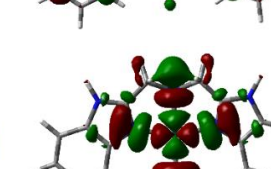**Figure S32:** Molecular structure of **Pdl₂**
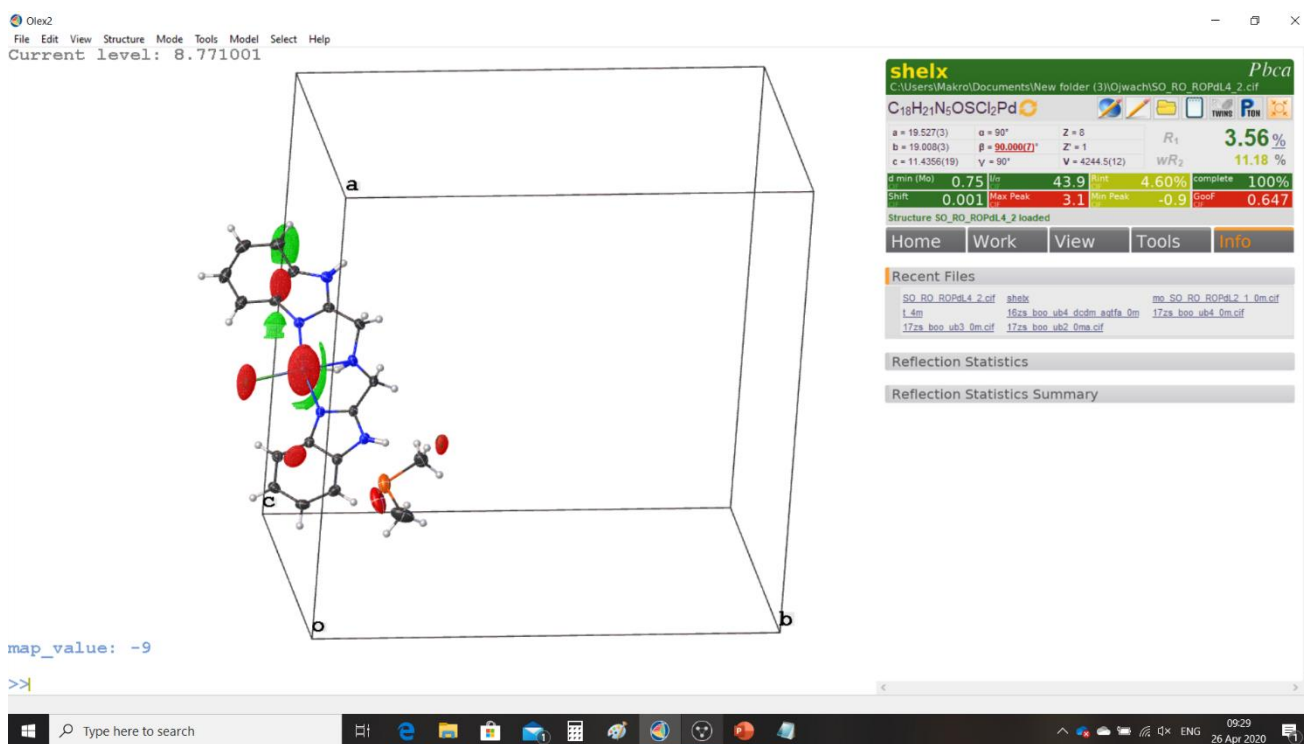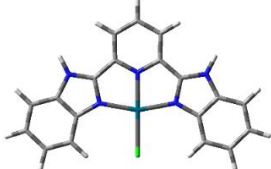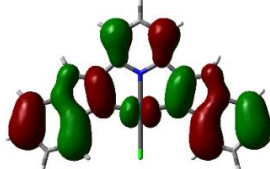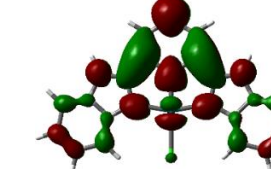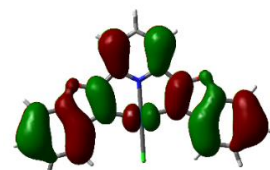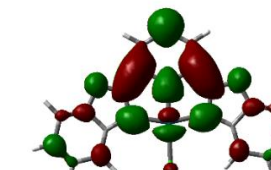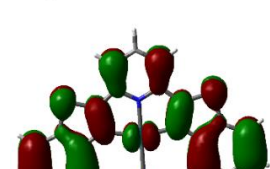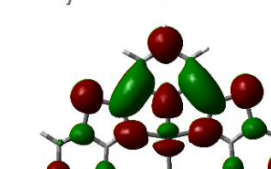
Figure S33: Molecular structure of **PdL₄**

Table S1: Summary of the crystallographic data and structure refinement for complexes **PdL₂** and **PdL₄.**

Parameter	PdL₂	PdL₄
Empirical formula	C21H14BClF4N4O2Pd	C18 H21 Cl2 N5 O Pd S
Formula weight	583.02	532.76
Temperature	100 (2) K	101(2) K
Wavelength	0.71073 Å	0.71073 Å
Crystal system	Monoclinic	Orthorhombic
Space group	P 21/c	P b c a
Unit cell dimensions		
a (Å)	6.6715(4)	19.527(3)
b (Å)	12.8094(7)	19.008(3)
c (Å)	24.5913(14)	11.4356(19)
α (°)	90	90
β (°)	91.713(2)	90.000(7)
γ (°)	90	90
Volume	2100.6(2) Å³	4244.5(12) Å³
Z	4	8
Density (calculated)	1.844 Mg/m³	1.667 Mg/m³
Absorption coefficient	1. 075 mm⁻¹	1.244 mm⁻¹
F(000)	1152.0	2144
Crystal size	0.220 x 0.180 x 0.150 mm³	0.800 x 0.240 x 0.160 mm³
Theta range for data collection	1.657 to 28.985°.	2.086 to 28.377°.

Table S2: DFT optimised HOMO, LUMO frontier molecular orbitals, with respective planarity structures of Pd(II) complexes at B3LYP/LANL2DZ theory level (Iso value = 0.02)

Complex	Optimised structure	HOMO map	LUMO map	planarity
PdL$_1$				
PdL$_2$				
PdL$_3$				
PdL$_4$				

The DFT optimised structures reveal that the electron densities of the HOMO orbitals are predominately contributed by the *4d*-orbitals of Pd(II) metal centre and the π-system of the entire inert ligand architecture, and in the case of **PdL$_4$** the electrons are also contributed by the 3p-orbitals of the chlorine atoms. On the other hand, the LUMO electron clouds are mainly localised on the pyridyl ligand moiety and Pd(II) ion, and in the case of **PdL$_4$**, the electrons are also distributed on the chloride atom. The planarity around the Pd(II) metal centre, as made possible through the in-plane pyridine/benzoazole ligand system, seems to offer little or no steric hindrance to the incoming nucleophile in **PdL$_1$**, **PdL$_2$**, and **PdL$_3$**. Conversely, the auxiliary ligand in **PdL$_4$** suffers a slight distortion from planarity with the absence of the pyridine ring.

Table S3: Summary of selected computational data for the investigated complexes

Complexes	PdL$_1$	PdL$_2$	PdL$_3$	PdL$_4$
NBO Charges				
Pd^{2+}	0.675	0.619	0.549	0.482
Cl$^-$	-0.508	-0.485	-0.496	-0.505
N$_{trans}$ to Cl	-0.427	-0.427	-0.427	-0.636
N$_{cis}$ to Cl	-0.513	-0.497	-0.478	-0.540
X = Heteroatom	-0.548	-0.499	0.416	-0.557
Bond lengths (Å)				
TransN-Pd-Cl	179.98	179.99	178.00	171.49
HOMO-LUMO energy / eV				
LUMO/eV	-3.693	-3.514	-3.233	-2.754
HOMO/eV	-7.190	-7.084	-6.848	-6.750
ΔE/eV	3.497	3.570	3.615	3.996
Chemical hardness (η)	1.749	1.785	1.807	1.9982
Chemical softness (σ)	0.572	0.560	0.553	0.501
Electronic chemical potential (μ)	-5.442	-5.299	-5.040	-4.752
Electrophilicity index (ω)	8.468	7.864	7.028	5.651
Dipole moment (Debye)	15.552	13.733	12.946	11.086

The slight increase in the HOMO energy level across the series of Pd(II) complexes, indicates that electron donation density around Pd(II) metal increases, while the increase on the LUMO energy in a similar fashion demonstrates a reduction in π-acceptability of the ligand system in the complexes. The computed energy gap, ΔE$_{LUMO-HOMO}$ gradually increases from **PdL$_1$** to **PdL$_4$**.It is noticed that the LUMO energies of **PdL$_1$**-**PdL$_3$** are raised in the increasing order of the electronegativity of the heteroatom on the spectator ligand. This indicates that the HOMOs are stabilised and LUMOs are destabilised, as a result smaller ΔE$_{LUMO-HOMO}$ causing an observed decrease in reactivity. It is clear that **PdL$_4$** shows relatively high ΔE$_{LUMO-HOMO}$ when compared to **PdL$_1$**.This can be attributed to the absence of pyridine ring on the head of the ligand system on **PdL$_4$**, which indicates the absence of π-back bonding.
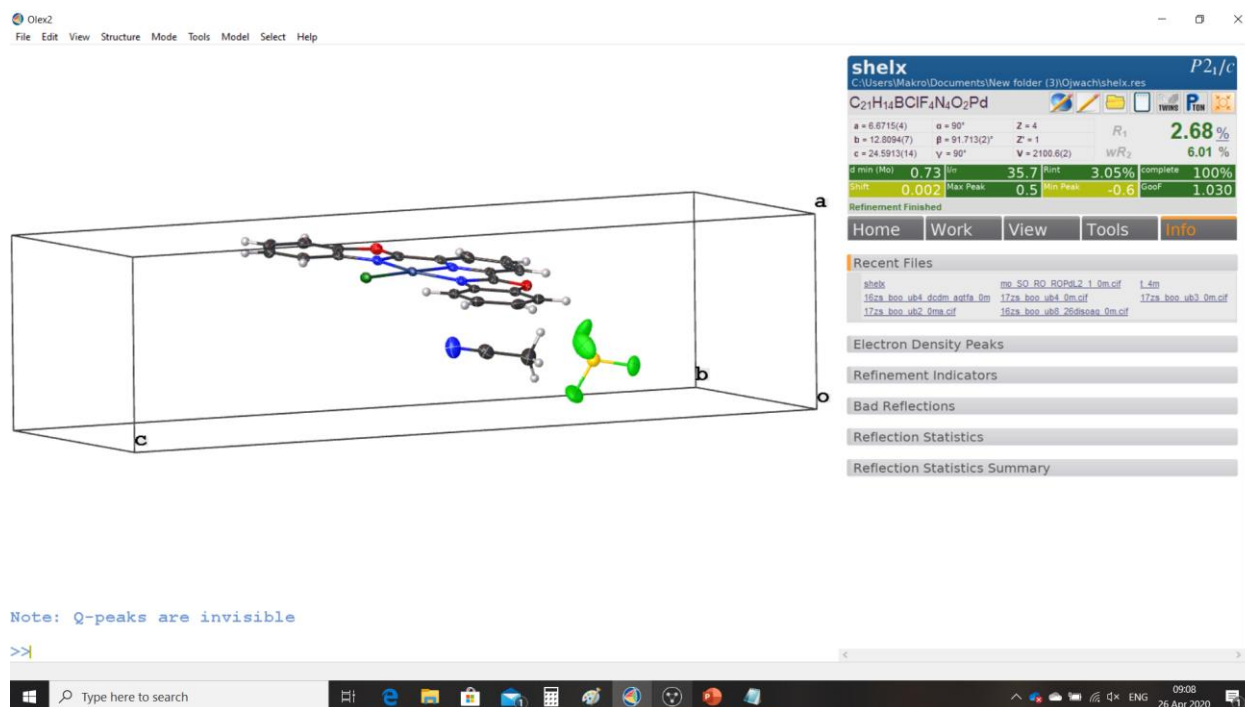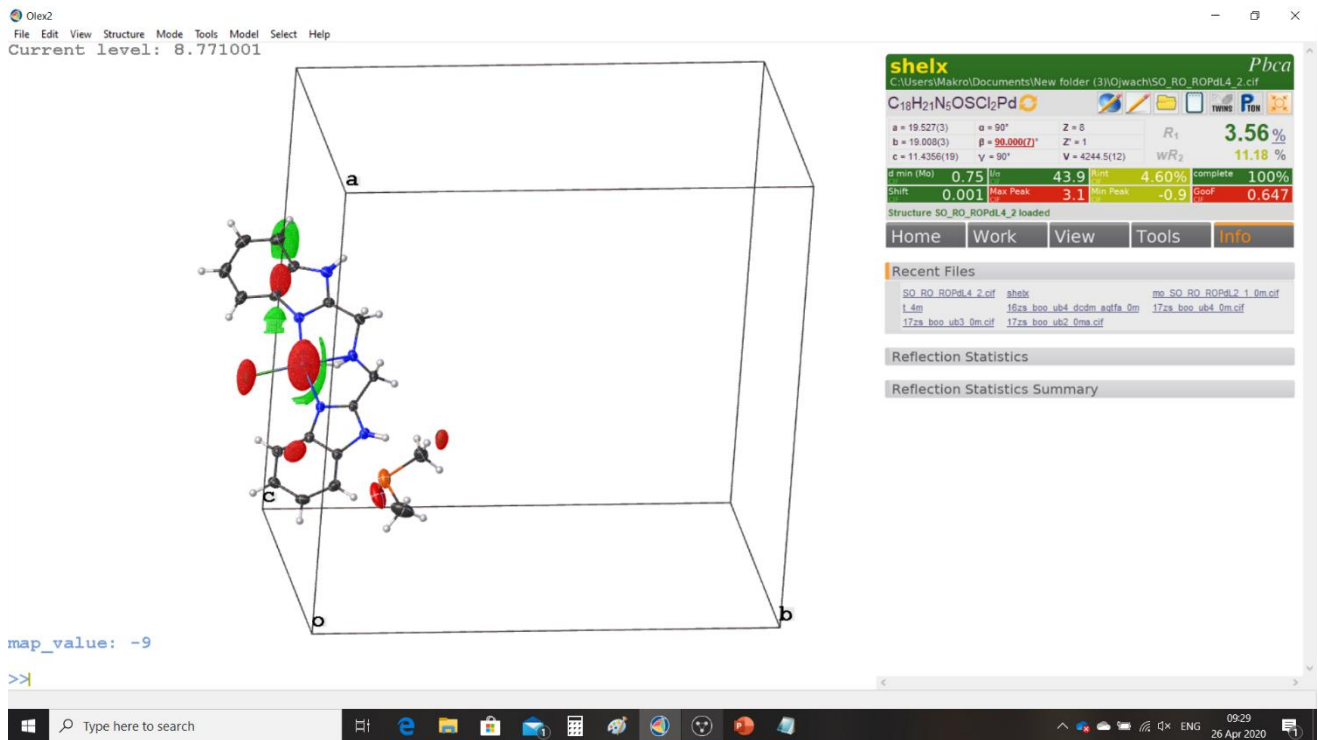
Figure S32: Molecular structure of **Pdl₂**

Figure S33: Molecular structure of **PdL₄**